ISSN 2347 - 3037

Indian Journal of Tribology

Volume 7 Number 3 July 2019

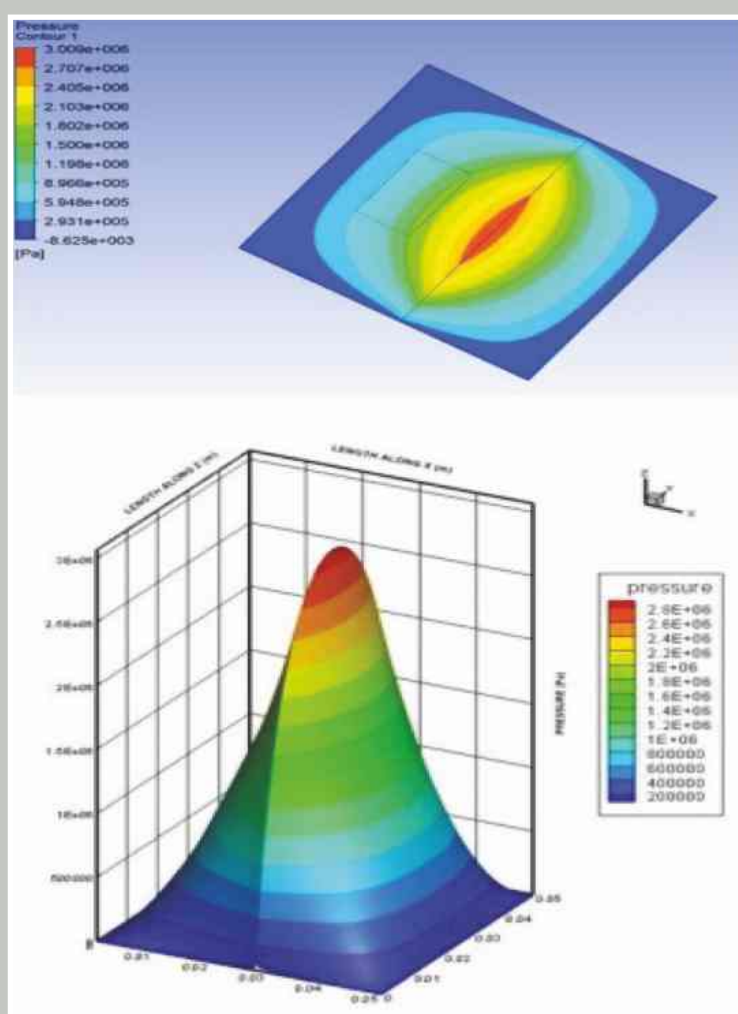

Printed on Behalf of the
Tribology Society of India
(Affiliated the the International Tribology Council (UK))
C/o. Indian Oil Corporation Ltd.
R&D Centre, Sector-13., Faridabad. HARYANA
Phone no: +91-129-2294264
E-mail : info@tribologyindia.org

Indian Journal of Tribology
ISSN 2347 - 3037
Vol. 7, No. 3, July 2019

Contents

Editor's Message

The Indian Journal of Tribology is coming out after a longer gap than usual. My apologies for this. While a lot of excuses can be given, nothing is going to matter. We do hope to get issues more regularly. For this the help of the tribology fraternity of India is required. This can happen when quality papers are submitted. I once again request you to have a look at the templates given in the website of the Tribology Society of India and follow the instructions for writing papers.

One of the developments that will be taking place this year is the hosting of IndiaTrib 2019 at the Indian Institute of Science, Bangalore. The event will be from the 1st to 4th of December 2019. The event will have 18 Plenary and Keynote speakers. More than 220 abstracts have been received by the deadline that was the end of July. This event is a packed event and will see some of the best tribologists around the world present their work. All of you are requested to come for this event andgive publicity to this event among your colleagues and contacts. This is possibly a once in a lifetime event to meet many of the well-known tribologists from around the world.

Raising the standard of tribology research in India and this research having an impact on sustainable development is the goal that we need to achieve. Please help us in the endeavor.

Satish V. Kailas

DRY SLIDING WEAR CHARACTERISTICS OF ALUMINUM ALLOY 8011/AlB_2 IN-SITU COMPOSITE

S. K. Singh[1], N. Kumar [1*], G. Gautam[2], A.K. Padap[1], A. Mohan[3], R. K. Gautam[4] and S. Mohan[5]
[1]Department of Mechanical Engineering, B.I.E.T, Jhansi, India
[2]Department of Metallurgical Engineering, I.I.T, Roorkee, India
[3]Department of Physics, I.I.T (BHU), Varanasi, India
[4]Department of Mechanical Engineering, I.I.T (BHU), Varanasi, India
[5]Department of Metallurgical Engineering, I.I.T (BHU), Varanasi, India
*Corresponding author (E-mail: narendra.dharwan@gmail.com)

KEY WORDS: ‘8011 alloy’, ‘stir casting’, ‘AlB_2’,‘in-situ’,‘wear’

ABSTRACT

Al 8011alloy has been reinforced with 6 vol. % of aluminum diboride (AlB_2) particles by in-situ synthesis process to prepare 8011/AlB_2 composite.Composite was characterized by XRD, Optical microscopy, Scanning Electron Microscopy (SEM) hardness and wear studies. AlB_2 particles were identified by XRD analysis. Microstructural studies reveal the morphology and distribution of AlB_2 particles. Enhancement in hardness was observed due to the presence of AlB_2 particles in the matrix. Wear results reveal that composite has lower wear rate than unreinforced alloy sliding under same sliding conditions. Worn surfaces examined under SEM reveals the mode of wear involved.

1. INTRODUCTION

Aluminum matrix composites (AMCs) are widely used because of high stiffness, high strength to weight ratio, low coefficient of thermal expansion and good wear resistance as compared their conventional alloys [1]. In-situ technique is mostly used to prepare AMCs as it offers some advantages over ex-situ process such as finer particle, homogeneity, isotropy, better thermal stability and simple to adopt [2].

Some studies are done in past by using Al8011 alloy as matrix and AlB_2 as reinforcement materials to improve the properties of alloy. Vembu and Ganesan [3] synthesized Al8011/15% SiC_p composite through stir casting and optimized the aging parameters to obtain maximum strength and hardness. Karthik kumar et al. [4] also reported improvement in mechanical properties with the addition of B_4C and red mud particles into Al 8011 alloy. Deppisch et al. [5] prepared high purity AlB_2 flake reinforced aluminum matrix composite by melting. In-situ liquid heat treatment was applied to produce AlB_2 flakes in the matrix. In another study Deppisch et al. [6] analysedthe crystallization and growth behavior of AlB_2 flakes in aluminum matrix. Ficici et al. [7] studieddry sliding wear behavior of in-situ $AlB_{(2)}$/Al metal matrix composite. Koksal et al. [8] developed wear rate prediction model for wear using Taguchi’s technique in terms of wear parameters sliding velocity, normal load, sliding distance and reinforcement ratio. Moldovan et al. [9] developed 3 wt % AlBx (x=2,12) /AA6060/AlB_2, and AA5083 composite through in-situ technique using KBF_4 powder. Developed composites show higher resistance to crack initiation than unreinforced alloy. Recently Radhika and Raghu [10] studied the mechanical and abrasive wear behavior of functionally graded Al/AlB_2 composite by centrifugal casting.In the present study an effort is made to prepare the Al/AlB_2 composites by in-situ technique and to study its microstructure and dry sliding wear characteristics.

2. EXPERIMENTAL DETAILS

Al 8011alloy (Cu 0.001%, Mg 0.04%, Si 0.67%, Mn 0.002%, Zn 0.0028%, Pb 0.001%, Fe 1.01%, rest aluminium) and potassium tetra flouro borate (KBF_4) having purity of 96% salt are used as raw materials to prepare Al8011/AlB_2 aluminum matrix composite. In-situ reaction takes place at 850^0C between aluminum and KBF_4 as per Equation (1). Required amount aluminum and salt were melted at 850^0C to form 6 vol. % AlB_2 particles. Composite melt was stirred intermittently to get uniform distribution of AlB_2 particles. After degassing the melt was poured into preheated (200^0C) steel mold and kept to solidify naturally.

XRD (Rigaku), Optical microscope (Leitz Metallux-3) and SEM (ZEISS), model EVO 18, are used for phase and microstructure examination. Vickers Hardness tester (LIECA) is used to measure the hardness of prepared samples. Sliding wear test was conducted on pin-on-disc apparatus (DUCOM) at ambient temperature for different applied loads 10, 20 and 30N at fixed sliding distance and sliding velocity 2.7 Km and 1.5 m/s respectively.

$$3Al + 2KBF_4 \rightarrow AlB_2 + 2KF + 2AlF_3 \quad (1)$$

3. RESULTS AND DISCUSSION

3.1 XRD and Microstructural Examination

XRD pattern of prepared composite is shown in Fig.1, in which AlB_2 diffraction peaks are identified. Presence of

AlB_2 peaks is the confirmation of formation of particles in the aluminum matrix.

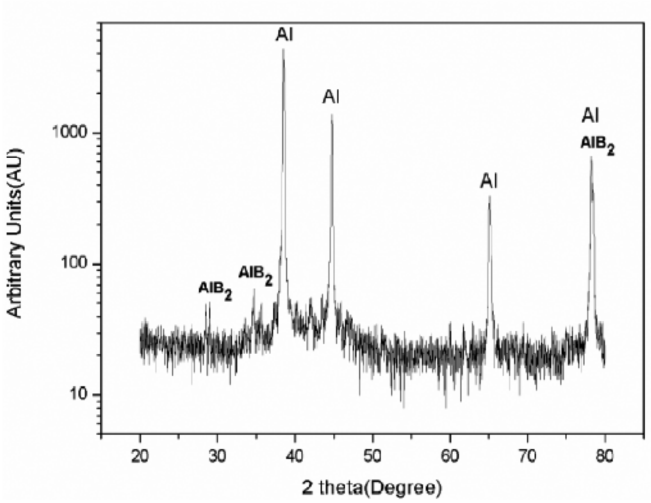

Fig. 1: XRD pattern of prepared composite

Optical micrograph (Fig. 2) of composite shows AlB_2 particles present in the matrix. In order to have adetail idea about morphology and distribution of AlB_2, SEM examination is carried out. AlB_2 particles are distributed in the matrix and observed in flakes and hexagonal shapes in the size range of 2.5 mm to 10 mm. (Fig. 3a-b),

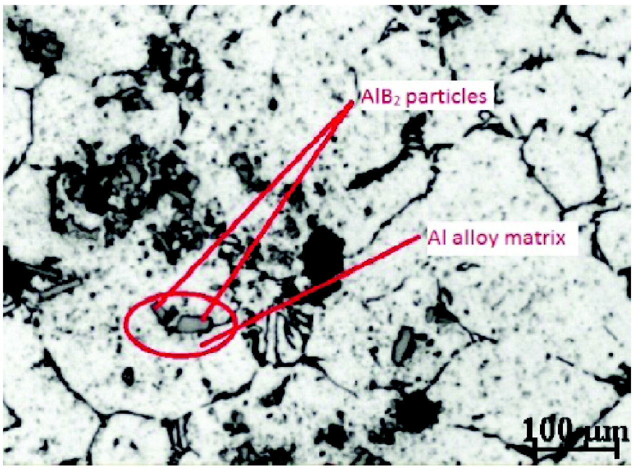

Fig. 2: Optical micrograph of 8011/AlB_2 composite

3.2 Hardness Measurement

Vickers's hardness is measured at 1 Kg load and 10 seconds dwell time. Hardness of composite was observed to be improved by 19.5% as compared to base alloy. This is attributed to the presence of hard particles in the soft aluminum matrix.

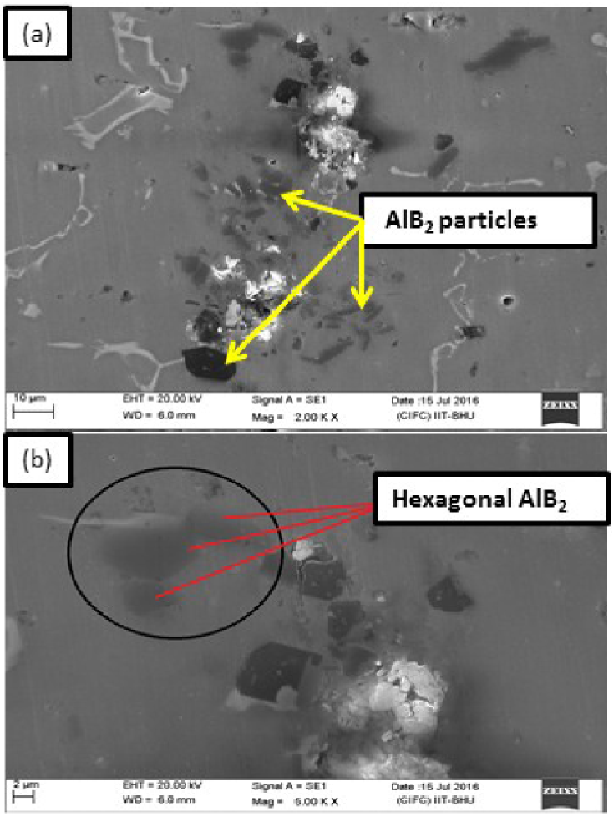

Fig. 3: SEM micrograph showing (a) distribution and morphology of AlB_2 particle

3.3 Wear Characteristics

Figure 4 shows variation of weight loss with applied load for base alloy and Al 8011/6 vol. % AlB_2 composite. It is observed that weight loss increases with increase in applied load for both the alloy and composite. The possible reason for increased weight loss may be due to increase in contact area between the two surfaces with increase in load, which results into generation of large amount of frictional heat.Frictional heating leads to softening of the pin sample and therefore hard asperities penetrate deeply into soft pin surface and weight loss increases [2].

However the weight loss of composite is lower as compared to alloy. The reduced weight loss is attributed to AlB_2 particles which enhanced hardness and strength of composite.

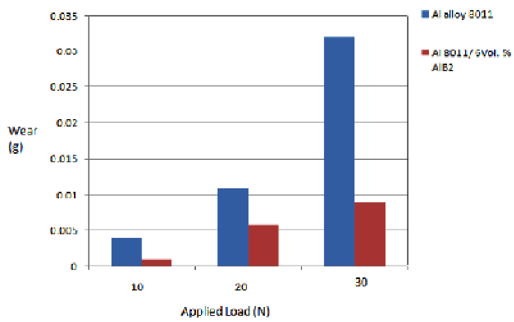

Fig. 4: Variation of weight loss with applied load

Figure 5 a-b shows the worn surface morphology of alloy and composite at 10 N load after sliding 2.7 km at sliding velocity of 1.5m/s.At low loadworn surface shows relatively smooth areas with shallow grooves, on the both the samplesand wear mode is oxidative but as the load increase to 30 N oxidative mode changes to metallic and wear surface exhibits deep grooves, severely damaged areas, and delamination which leads to the increased wear loss (Fig. 6 a-b).

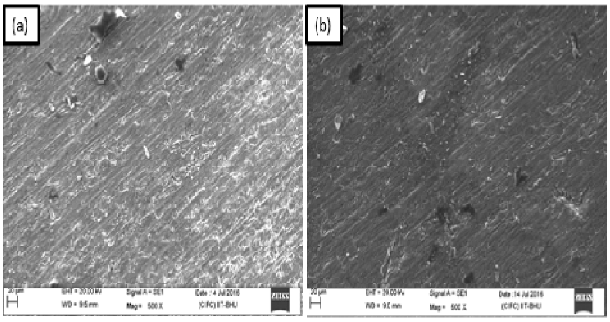

Fig. 5: Worn surface of (a) base alloy (b) Al8011/6 vol. % AlB_2 composite at 10 N load

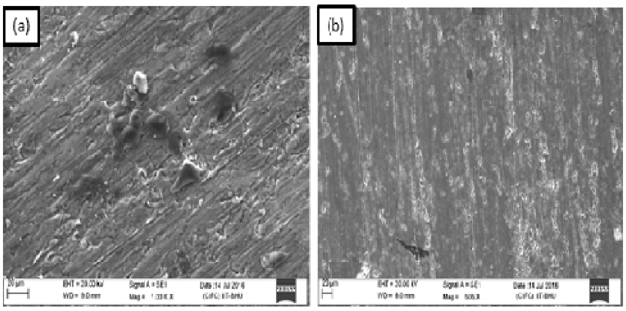

Fig. 6: Worn surface of (a) base alloy (b) Al8011/6 vol. % AlB_2 composite at 30 N load

4. CONCLUSION

i. In-situ process has been successfully employed to prepare the Al 8011/6 vol. % AlB_2 composite.

ii. XRD analysis confirms the presence of AlB_2 particles in the aluminum matrix.

iii. AlB_2 particles are observed in hexagonal and flakes morphology with greyish color in the size range of 2.5 mm to 10 mm.

iv. Vickers hardness of the composite is improved by 19.5% when compared to base alloy.

v. Weight loss of composite is less as compared to base alloy operating under same sliding conditions which concludes its reduced wear rate.

vi. Oxidative wear mode is dominated at low load and converted to metallic as the load increases.

vii. Worn surface morphology is in agreement with the wear results.

5. REFERENCES

[1] Yuan, L., Han, J., Liu, J. and Jiang, Z. Mechanical properties and tribological behavior of aluminum matrix composites reinforced with in-situ AlB_2 particles. Tribology International, 2016, Vol. 98, pp.41-47.

[2] Kumar, N., Gautam, G., Gautam, R.K., Mohan, A. and Mohan, S. Wear, friction and profilometer studies of insitu AA5052/ZrB_2 composites. Tribology International, 2016, Vol. 97, pp. 313-326.

[3] Vembu, V. and Ganesan, G. Heat treatment optimization for tensile properties of 8011Al/15%SiCp metal matrix composite using response surface methodology. Defence Technology, 2015, Vol. 11(4), pp.390-395.

[4] Karthikkumar, C., Baranirajan, R., Premnauth, I. and Manimaran, P. Investigations on mechanical properties of Al 8011 reinforced with micro B_4C/Red Mud by stir casting method. International Journal of Engineering Research and General Science, 2016, Vol.4(2)

[5] Deppisch, C., Liu, G., Shang, J.K. and Economy, J. Processing and mechanical properties of AlB2 flake reinforced Al-alloy composites. Materials Science and Engineering: A, 1997, Vol. 225(1-2), pp.153-161.

[6] Deppisch, C., Liu, G., Hall, A., Xu, Y., Zangvil, A., Shang, J.K. and Economy, J.The crystallization and growth of AlB2 single crystal flakes in aluminum. Journal of materials research, 1998, Vol. 13(12), pp. 3485-3498.

[7] Ficici, F., Koksal, S., Kayikci, R. and Savas, O. Investigation of unlubricated sliding wear behaviours of in-situ AlB(2)/Al metal matrix composite. Advanced Composites Letters, 2011,Vol. 20(4), pp.109-116.

[8] Koksal, S., Ficici, F., Kayikci, R. and Savas, O. Experimental optimization of dry sliding wear behavior of in situ AlB_2/Al composite based on Taguchi's method. Materials & Design, 2012, Vol. 42, pp.124-130.

[9] Moldovan, P., Dragut, D.V., Butu, M., Besea, L.M. and Preda, E.A.In situ development of AlBx/AA6060 and AA5083 alloys cast composites. Composites Part B: Engineering, 2016, Vol. 97, pp.9-17.

[10] Radhika, N. and Raghu, R. Effect of abrasive medium on wear behavior of Al/AlB_2 functionally graded metal matrix composite. Tribology Online, 2016, Vol. 11(3), pp. 487-493.

THERMALLY SPRAYED CeO_2 DOPED Al_2O_3 COATING ON AZ91 ALLOY

Sanjeet Kumar and Deepak Kumar*

Industrial Tribology, Machine Dynamics and Maintenance Engineering Centre
Indian Institute of Technology, Delhi, New Delhi, India
*Corresponding author (E-mail: dkumar@itmmec.iitd.ac.in)

KEY WORDS: Mg alloy, D-gun spray, scratch test

ABSTRACT

The tribological use of Mg-alloys can be promoted in many applications by protecting them against corrosion and wear. Localized protection of contacting surface helps in reduction of wear and corrosion as they are surface related phenomenon. Present study deals with the development of ceramic based coatings on AZ91 alloy using thermal spray. The Al_2O_3 and Al_2O_3 doped with CeO_2 were deposited on AZ91 alloy using D-gun spray and contribution of ceria in enhancement of tribological and mechanical properties is investigated. The surface and subsurface characterization was done prior and post experiments using SEM/EDS. Further, the metallurgical characteristics of coatings were recorded using the X-ray diffractometer and tribological responses were studied using tribometer. The scratch resistance of the coatings was tested under the ramp load. The CeO_2 doped Al_2O_3 coated AZ91 alloy showed better properties as compare to the bare and Al_2O_3 coated AZ91 alloy. The improvements can be attributed to the refined microstructure and increased hardness. It can be suggested that ceria plays an important role in enhancing the lubricity of coating and tribological properties.

1. INTRODUCTION

AZ91 Mg alloys are being preferred over the other Mg alloys due to their good castability, cheap prices and suitable mechanical and corrosion properties under room temperature conditions. They are widely used in the form of die casted thin components which can be operated in the range of 110-125°C due to their limited corrosion and wear resistance [1], [2]. Therefore, there is need to improve the wear and corrosion properties of the alloy so as to extend its use, beyond limitation, in various industrial applications. Many efforts have been made by various researchers to overcome the limitations [3]–[6]. There are various methods which can be explored such as alloying, surface treatment and heat treatment to impart favorable properties to the Mg-alloys [7]. One of the method to enhance the mechanical and tribological properties of the material is surface coatings. Surface modification of Mg-alloys can be done by depositing or producing various coatings or layers of either similar or dissimilar material. Surface coating technologies such as chemical vapor deposition (CVD) [8], [9], physical vapor deposition (PVD) [8]–[10], electro-deposition [11], [12], micro-arc oxidation [3], [11], thermal spray [13], [14], cold spray [14], [15] have been developed to extend the use of Mg-alloys in different industries. The surface properties can be altered by developing the coating with high hardness, refined microstructure, high adhesion strength etc. and can be achieved by thermal spray techniques such as HVOF, plasma spray etc. [16].

In recent years, rare earth elements (REE) have been successfully employed to enhance the wear and corrosion resistance by influencing the microstructure [17]. Zhang et al. [18] developed rare earth metals and Ni-based coatings using supersonic plasma spray technique. They observed that the addition of rare earth elements resulted in increase of wear resistant.

They explored the surface microstructures and suggested that it was more compact and less porous. Rare earth, being possession of purifying and refining properties they also exhibits excellent tribological and mechanical properties and hence, suitable for engineering the surfaces[18]. In an investigation made by Wang et al. [19]it was observed that deposition of ceramic coating on Mg alloy gives rise to increase in hardness and anticorrosion properties Sharma [16] carried out a study by depositing CeO_2 doped Ni/WC based coating via HVOF technique and observed that there is an improvement in wear resistance. They found that addition of CeO_2 played an important role in enhancing the wear resistance by increasing the hardness of coatings. Liu et al. [20] also investigated the effect of CeO_2 addition in HVOF sprayed WC-12wt. %Co coating. They reported that the CeO_2 doped coating was the less porous than undoped ones and the mechanical properties were improved.

In this study, tribological behavior of bare and coated AZ91 alloy is investigated by depositing the D-gun spray. Al_2O_3 and Al_2O_3+0.4% CeO_2 coatings are deposited on AZ91 alloy. The scratch resistance and friction behavior of the coatings were recorded under tribometer. The samples were characterized using microhardness tester and SEM/EDS respectively. Further, contact angle measurements and surface energy of the samples were also recorded to comment on the nature of the surfaces.

2. EXPERIMENTAL

2.1 Methods and Materials

The base materials selected for study were cast magnesium alloy AZ91 (Mg-9wt.%Al-1wt.%Zn) and near eutectic Al-11.3%Si (Al-11.3wt.%Si-0.7wt.%Fe-1.8wt.%Cu-0.2wt.%Mn-0.6wt.%Zn-0.2wt.%Mg) alloy. The cast AZ91 Mg alloy was procured from XI'anYuechen Metal Products Co., Ltd. China. Whereas, the near eutectic Al-11.3% alloy was supplied by Ye Chiu, Malaysia.

The samples having dimensions 10 mm x 10mm x 50 mm were cut from the as cast AZ91 Mg alloy block. The near eutectic Al-11.3%Si alloy samples having dimensions 20 mm x 40 mm x 6 mm were cut from the as cast shaft. All the samples were cut using electro discharge machining (EDM) wire cut. These samples were further polished using 400, 600, 800, 1000 and 2500 grit size emery paper followed by the cloth polishing with Al_2O_3 having particle size 1 µm.

The Al_2O_3 and Al_2O_3 doped with 0.4wt.%CeO_2 coatings were deposited on AZ91 Mg alloy using D-gun thermal spray technique. The coatings were deposited at SVX 'M' Surface Engineering, Noida, India. The parameters of spray gun were kept constant as shown in Table 1.

Table1. D-gun process parameters

Gases	Pressure (MPa)
Oxygen	0.2
Acetylene	0.14
Nitrogen	0.4
Consumption of powder per shot	0.05-0.02 g/shot
Water consumption rate	15-25 liter/minute
Firing rate	3 shot/s
Coating thickness per shot	25-30 µm
Spraying distance	165 mm

Prior to coating, the powders were ball milled for 8 h in order to achieve the homogeneous dispersion. The rpm of the ball mill was 70 (approximately) and kept constant. The samples were grit blasted prior to coating deposition to increase the surface roughness and hence increase the substrate – coating adherence.

3. RESULTS AND DISCUSSION

3.1. Microstructure

The as sprayed morphology of Al_2O_3 and Al_2O_3+0.4%CeO_2 coatings are shown in Fig. 1. The CeO_2 doped Al_2O_3 coating (Fig. 1b) shows more intact, uniform and dense microstructure as compare to pure Al_2O_3 coating. The intactness and refined microstructure of CeO_2 doped coating can be attributed to the rare earth effect; which alters the microstructure by repositioning of Ce sites.

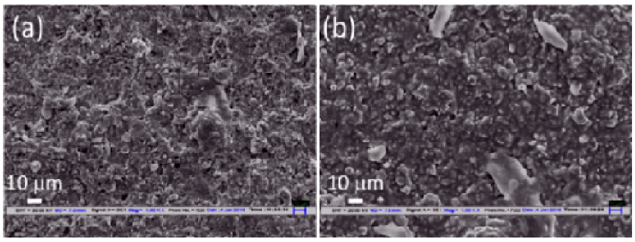

Fig. 1: SEM micrograph of as sprayed (a) Al_2O_3 and (b) Al_2O_3+0.4%CeO_2 coating respectively

Fig. 2 and Fig. 3 shows the SEM micrograph of polished Al_2O_3 and Al_2O_3 + 0.4wt.% CeO_2 coated AZ91 alloy along with their corresponding X-ray mapping.

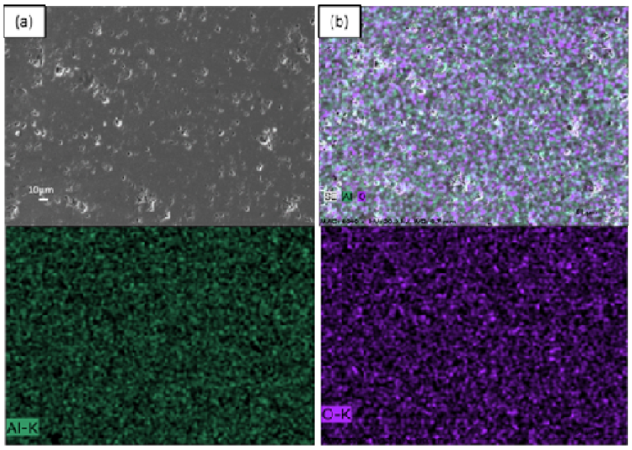

Fig. 2: SEM micrograph of polished Al_2O_3 coated AZ91 alloy along with corresponding X-ray mapping

Fig. 3 shows the X-ray mapping of Al_2O_3 + 0.4wt.%CeO_2 in which the uniform distribution of CeO_2 can be observed. Also, the CeO_2 doped coating (Fig. 3) contains less porosity and defects as compared to the undoped (Fig. 2) one.

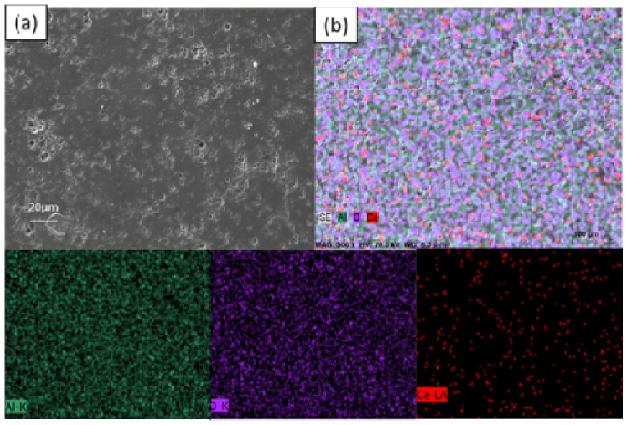

Fig. 3: SEM micrograph of polished Al_2O_3 + 0.4wt.% CeO_2 coated AZ91 alloy along with corresponding X-ray mapping

CeO_2 plays an important role in controlling the microstructure of the coating by the mechanism of site occupancy at grain boundary [21]in large amount and more grain formation as well.

3.2 Hardness

The microhardness of both the coating was recorded and is summarized in Table 2.

Table. 2 Microhardness at various regions

Region	Microhardness, GPa	
	Al_2O_3 Coating	Al_2O_3+0.4wt. % CeO_2 Coating
Top surface	14.2±0.30	15.8±0.63
Coating (Cross-sectional)	8.86±0.26	10.4±0.44
At interface	6.3± 0.29	6.7± 0.64
At substrate	0.82±0.06	0.81±0.03

It can be observed from the Table 2 that the top surface have attained the high hardness as compared to the cross-section of coating. The reduction of hardness from top to the cross-sectional coating can be justified by the layered structure of the coatings (Fig. 4). This can be further explained by the slipping phenomenon that might have occurred between the inter layers.

On the other hand, the increase in hardness due to CeO_2 doping can be attributed to the microstructural refinement and the segregation of the CeO_2 at the grain boundary[21] which led to generate stresses at the boundary and ultimately leading to the increase in hardness and hence imparting the mechanical and tribological properties as well.

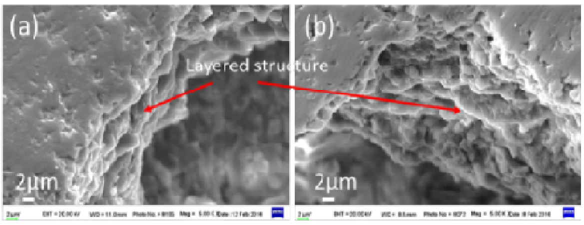

Fig. 4: SEM micrograph showing layered structure of the (a) Al_2O_3 and (b) Al_2O_3+0.4%CeO_2 coating respectively

3.3 Scratch test

The scratch test of Al_2O_3 and Al_2O_3+0.4%CeO_2 coating was performed on tribometer, under the ramp load of 5-25 N. The ramp load was applied for the 30 s. The SEM micrograph of the scratched coatings is shown in Fig. 5. Fig. 5 shows that the scratch resistance of both the coatings was high as no peeling or complete delamination observed under the load range of 5-25N. Although, Al_2O_3 coating (Fig. 5a) exhibits the little bit high damage as compared to Al_2O_3+0.4%CeO_2 coating (Fig. 5b).

As the indenter scratches at high load i.e. towards 25N, the failure of coating along one side of the groove can be noticed (Fig. 5a), which is absent for Al_2O_3+0.4%CeO_2 coating. The heap of detached particles can be observed in case of Al_2O_3 coating which is not in the case of Al_2O_3+0.4%CeO_2 coating. The increase in scratch resistance of Al_2O_3+0.4%CeO_2 coating can be attributed due to the combined effect of microstructural and mechanical properties improvement as imparted by the dopingof CeO_2.

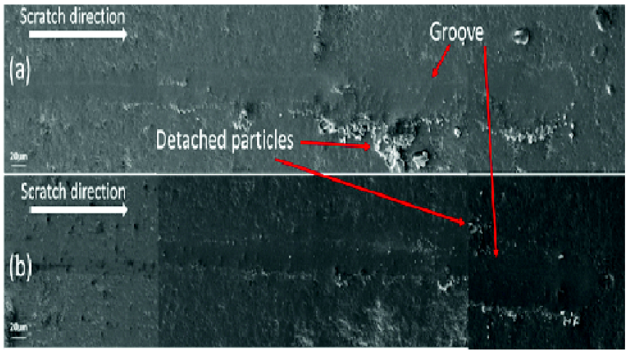

Fig. 5: SEM micrograph showing the scratch on (a) Al_2O_3 and (b) Al_2O_3+0.4% CeO_2 coating under the load of 5-25N respectively

3.3 Contact angle and surface energy

The contact angle was measured using DI (de-ionized) water with sessile drop method and each drop consisted 2 µl volume with dosing rate of 0.16 µl/s. The Al_2O_3 coating consisted the water contact angle of 55° whereas the CeO_2 doped Al_2O_3 coating recorded the angle close to 80°. It has been reported by Azimi et al. [22] that rare earth oxides shows hydrophobicity due to their electronic structural arrangement. The surface free energy of the bare and coated samples were estimated using Young-Dupre method and found to be; 33.12mJ/m^2, 29.47 mJ/m^2 and 29.40 mJ/m^2 for bare, Al_2O_3 coated and CeO_2 doped Al_2O_3 coated AZ91 respectively. It was also observed that the reduction in surface energies was majorly due to decrease in polar component.

3.4 Friction and wear behavior

Fig.6 shows the coefficient of friction behavior of bare, Al_2O_3 and Al_2O_3+0.4% CeO_2 coated AZ91 alloy. The effect of ceria doping can be clearly seen as CeO_2 doped Al_2O_3

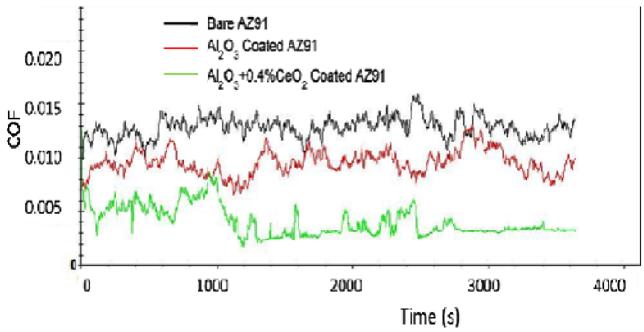

Fig. 6:Variation of coefficient of friction of bare, Al_2O_3 coated and Al_2O_3+0.4%CeO_2 coated AZ91 alloy when slid against near eutectic Al-11.3%Si alloy under the 20 N load and 0.05m/s sliding velocity

coated AZ91 alloy exhibits the lowest coefficient of friction followed by Al_2O_3 coated and bare AZ91 alloy. The reduction in coefficient of friction may be attributed to the rare earth effect by which the CeO_2 has contributed to increase in hardness and provide lubricating effect, since CeO_2 imparted the tribological properties.

The improved tribological response of CeO_2 doped coating can be attributed to the refined microstructure. It is reported that the addition of CeO_2 led to dense and compact microstructure [18]. Due to increase in hardness the penetration depth will be less and hence the formation of fine groove. This leads to reduction in effective contact area hence reduced coefficient of friction [16]. It has been reported in literature that the friction behaviour of the tribopair depends on the wettability of the surface by lubricant[23]. Pawlak et al. concluded that the tribology of the contact surfaces can be controlled by controlling the surface energies [24].

As far as wear is considered, the coated specimen showed no wear under the constant load of 20 N with sliding velocity of 0.05 m/s. Although, bare specimen recorded the wear rate of 3.41 x 10^{-4} mm^3/N-m. On the other hand the counter surfaces showed the wear rate in the range of (1.04 – 1.8) x 10^{-4} mm^3/N-m when slid against bare and coated AZ91 alloy. The Al_2O_3 based ceramic coatings showed better wear resistance as compared to that of bare alloy.

4. CONCLUSIONS

The CeO_2 doped Al_2O_3 coating showed the better tribological properties as compared to that of Al_2O_3 coated and bare AZ91 alloy. The rare earth ceria has played an important role in improving the hardness, scratch resistance and frictional behavior of AZ91 alloy. The following conclusions can be made from the tribological study investigated:

1. The Al_2O_3 based ceramic coatings can be deposited on AZ91 alloy using D-gun spray technique.
2. The rare earth oxide i.e. CeO_2 played important role in refining the microstructure of Al_2O_3 coatings by grain growth mechanism.
3. The CeO_2 doping led to increase the hardness of the coating and hence controlling the tribology of the coatings. CeO_2 doped Al_2O_3 coating recorded the lowest coefficient of friction.
4. The contact angle and surface/interfacial energies also plays in controlling the tribology behavior of the tribopair by decrease in polar component of the surface energy in CeO_2 doped Al_2O_3 coating.

5. REFERENCES

[1] A. Zafari, H. M. Ghasemi, and R. Mahmudi, “An investigation on the tribological behavior of AZ91 and AZ91+3wt% RE magnesium alloys at elevated temperatures,” *Mater. Des.*, vol. 54, pp. 544–552, 2014.

[2] X. Zhong, Q. Li, J. Hu, and Y. Lu, “Characterization and corrosion studies of ceria thin film based on fluorinated AZ91D magnesium alloy,” *Corros. Sci.*, vol. 50, no. 8, pp. 2304–2309, Aug. 2008.

[3] J. Zhang, C. Dai, J. Wei, Z. Wen, S. Zhang, and C. Chen, “Degradable behavior and bioactivity of micro-arc oxidized AZ91D Mg alloy with calcium phosphate/ chitosan composite coating in m-SBF,” *Colloids Surfaces B Biointerfaces*, vol. 111, pp. 179–187, Jun. 2013.

[4] H. R. Bakhsheshi-Rad, E. Hamzah, M. Daroonparvar, M. a. M. Yajid, and M. Medraj, “Fabrication and corrosion behavior of Si/HA nano-composite coatings on biodegradable Mg–Zn–Mn–Ca alloy,” *Surf. Coatings Technol.*, vol. 258, pp. 1090–1099, Jul. 2014.

[5] B. J. Zheng, X. M. Chen, and J. S. Lian, “Microstructure and wear property of laser cladding Al+SiC powders on AZ91D magnesium alloy,” *Opt. Lasers Eng.*, vol. 48, no. 5, pp. 526–532, May 2010.

[6] K. Z. and P. J.-W. Kim Hyung-jin, “Enhanced adhesion of color coatings on Mg surfaces by Ion-beam mixing,” *J. Korean Phys. Soc.*, vol. 54, no. 5, pp. 2138–2142, 2009.

[7] H. S. Brar, I. S. Berglund, J. B. Allen, and M. V. Manuel, “The role of surface oxidation on the degradation behavior of biodegradable Mg-RE (Gd, Y, Sc) alloys for resorbable implants,” *Mater. Sci. Eng. C*, vol. 40, pp. 407–417, 2014.

[8] R. A. Antunes and M. C. L. de Oliveira, “Corrosion fatigue of biomedical metallic alloys: mechanisms and mitigation.,” *Acta Biomater.*, vol. 8, no. 3, pp. 937–62, Mar. 2012.

[9] K. Funatani, “Emerging technology in surface modification of light metals,” *Surf. Coatings Technol.*, vol. 133–134, pp. 264–272, 2000.

[10] G. Wu, W. Dai, H. Zheng, and A. Wang, “Improving wear resistance and corrosion resistance of AZ31 magnesium alloy by DLC/AlN/Al coating,” *Surf. Coatings Technol.*, vol. 205, no. 7, pp. 2067–2073, 2010.

[11] P. Liu, X. Pan, W. Yang, K. Cai, and Y. Chen, “Al2O3–ZrO2 ceramic coatings fabricated on WE43 magnesium alloy by cathodic plasma electrolytic deposition,” *Mater. Lett.*, vol. 70, pp. 16–18, Mar. 2012.

[12] C. Gu, J. Lian, J. He, Z. Jiang, and Q. Jiang, “High corrosion-resistance nanocrystalline Ni coating on AZ91D magnesium alloy,” *Surf. Coatings Technol.*, vol. 200, pp. 5413–5418, 2006.

[13] M. Campo, M. Carboneras, M. D. López, B. Torres, P. Rodrigo, E. Otero, and J. Rams, “Corrosion resistance of thermally sprayed Al and Al/SiC coatings on Mg,”

Surf. Coatings Technol., vol. 203, no. 20–21, pp. 3224–3230, Jul. 2009.

[14] X. Suo, X. Guo, W. Li, M. P. Planche, R. Bolot, H. Liao, and C. Coddet, "Preparation and characterization of magnesium coating deposited by cold spraying," *J. Mater. Process. Technol.*, vol. 212, no. 1, pp. 100–105, 2012.

[15] V. K. Champagne, D. Helfritch, and P. F. Leyman, "Magnesium repair by cold spray," *Plat. Surf. Finish.*, vol. 95, no. 9, pp. 19–28, 2008.

[16] S. Sharma, "Wear study of Ni–WC composite coating modified with CeO2," *Int. J. Adv. Manuf. Technol.*, vol. 61, no. 9–12, pp. 889–900, 2012.

[17] Z. Zhang, Z. Wang, B. Liang, and P. La, "Effects of CeO2 on friction and wear characteristics of Fe-Ni-Cr alloy coatings," *Tribol. Int.*, vol. 39, pp. 971–978, 2006.

[18] Z. Zhang, X. Lu, B. Han, and J. Luo, "Rare earth effect on the microstructure and wear resistance of Ni-based coatings," *Mater. Sci. Eng. A*, vol. 454–455, pp. 194–202, 2007.

[19] Y. Wang, D. Wei, J. Yu, and S. Di, "Effects of Al2O3 Nano-additive on Performance of Micro-arc Oxidation Coatings Formed on AZ91D Mg Alloy," *J. Mater. Sci. Technol.*, pp. 1–7, Mar. 2014.

[20] Y. Liu, G. Gou, X. Wang, Q. Jia, H. Chen, and M. Tu, "Effects of rare earth elements on the microstructure and mechanical properties of HVOF-sprayed WC-Co coatings," *J. Therm. Spray Technol.*, vol. 23, no. 7, pp. 1225–1231, 2014.

[21] Z. Zhang, B. Liang, and H. Guo, "The Effect of CeO2 Addition on the Microstructure and Properties of Ni-Based Flame-Spray Coatings.," *J. Therm. Spray Technol.*, vol. 23, no. 4, pp. 725–731, 2014.

[22] G. Azimi, R. Dhiman, H.-M. Kwon, A. T. Paxson, and K. K. Varanasi, "Hydrophobicity of rare-earth oxide ceramics.," *Nat. Mater.*, vol. 12, no. 4, pp. 315–20, Apr. 2013.

[23] M. Kalin and M. Polajnar, "The effect of wetting and surface energy on the friction and slip in oil-lubricated contacts," *Tribol. Lett.*, vol. 52, no. 2, pp. 185–194, 2013.

[24] Z. Pawlak, W. Urbaniak, and A. Oloyede, "The relationship between friction and wettability in aqueous environment," *Wear*, vol. 271, no. 9–10, pp. 1745–1749, 2011.

FRICTION, NOISE AND VIBRATIONAL RESPONSE OF REDUCED GRAPHENE OXIDE BLENDED LITHIUM GREASE UNDER THE POINT CONTACT

Jayant Singh[1*], Gautam Anand[1], Deepak Kumar, N. Tandon and Om P. Khatri[2]

[1]Industrial Tribology, Machine Dynamics and Maintenance Engineering Centre (ITMMEC), IIT Delhi, New Delhi 110016, India

[2]CSIR - Indian Institute of Petroleum, Dehradun, Uttrakhand, India

*Corresponding author (E-mail: singhjayant11@gmail.com)

ABSTRACT

Present study deals with the utilization of reduced Graphene oxide (rGO) as additive to grease and recording their effect on friction, vibration and noise. Nano-composite grease was prepared by dispersing rGO nano-sheets into commercial lithium base grease. The continuous supply of grease to the point contact is evaluated for ball-on-disc configuration for near rolling and rolling-sliding mixed motion by varying slide-roll-ratio percent (SRR %) under fixed load. Frictional response was recorded using elastohydrodymanic (EHD) rig. Recording of noise and vibration signals was carried out on EHD rig using sound analyzer and non-contact type capacitive transducer, respectively. The results show that there is an optimum concentration of rGO at which the levels of friction, noise and vibration are minimum. Almost 30 % reduction in friction coefficient was recorded along with suppression of many noise frequencies and reduction in level of vibrations.

1. INTRODUCTION

Greases are semi-solid lubricant and are composed of base oil, thickener and additives. Greases are characterized by three dimensional network of thickener fibers dispersed in base oil. The presence of these 3-D networks in greases enables them to behave more or less like a sponge (Cousseau, et al. [1]). Grease prompts to release oil during an application of mechanical stress and this oil is further reabsorbed on removal of the stresses (Huang, et al.[2]). Further, these 3-D fibrous structure of grease traps the additive particles ranging from nano to few microns in size.

The nanomaterials as additives to lubricants can significantly improve the tribological performance. Several nanomaterials have been exploited as additives for tribological applications including carbon nanotubes (Mohamed, et al. [3]), graphite powder (Zhang, et al. [4]) etc. It easily shears at the contact interfaces owing to lamellar structure and reduces the friction. Further, high mechanical strength of graphene provides excellent anti-wear property and load-bearing capacity. These few layers of graphene offer easy shearing. Present work is an attempt to explore the frictional response of nano-composite greases and establish the correlation with noise and vibration.

2. METHODOLOGY

Chrome steel (AISI 52100) was used disc and ball material of average surface roughness (Ra) around 0.01 ¼m. Ball and disc diameter were 19.05 mm and 100 mm respectively. Nano-composite grease was formulated using commercial Lithium grease. The nano-composite grease was formulated by dispersing rGO into grease. The rGO was prepared as reported by Mungse, et al. [5]. Prior to dispersion in to grease, the rGO was first sonicated in toluene for 1 hour to ensure the breakage of its agglomerates and larger sheets. The nano-composite grease was achieved by drop-wise addition of this dispersion into hot lithium grease (maintained at 110!) under heavy mechanical stirring. Mechanical stirring was done through magnetic stirrer for 45-50 minutes. Mixture is allowed to cool down to room temperature under normal environmental conditions to obtain desired nano-composite grease.

The structural features of rGO were probed with with XRD and HRTEM. The dispersion was characterized using DLS (Particulate Systems NanoPlus from Micromatrics, USA) and size of rGO distribution was estimated. The tribological evaluation of grease was done under ball-on-disc configuration using fully automated EHD rig (PCS Instruments, London). Experiments were performed by varying sliding speed from 0.3 m/s to 1.5 m/s at a constant load of 30 N. The rolling condition was constrained at slide-roll-ratio (SRR) of 3% and 27%. Sound pressure level (SPL) was measured to estimate the noise under 'A' weighting condition in decibels (dB) using sound analyzer (CEL-500 from CASELLA CEL LTD., UK). The microphone of sound analyzer was placed near to tribological contact by using tripod. Vibration signals were recorded using non-contact type capacitance based transducer also positioned near tribological contact. The vibration signals were passed through amplifier (Accumeasure 9000, by MTI Instruments Inc., USA) to display and store in FFT Analyzer CF-3200 (by ONOSOKKI Co. Ltd., Japan). The amplitudes of vibration signals were measured in terms of displacement.

3. RESULTS AND DISCUSSION

3.1 Characterization

The XRD pattern of rGO nano sheets (Fig. 1a) reveals very broad characteristic peak (002) centered at 2¸ = ~24.8°

owing to its lamellar structure and is corresponding of interlayer spacing (d) of ~0.35 nm. The ripples and folded regions are also seen in HRTEM image (Fig. 1b) of rGO nano sheets. Fig. 1c shows that there are some nano-sized particle of rGO along with micron size clusters.

3.2 Frictional response of greases

The difference in level of friction between rolling (3% SRR) and sliding-rolling (27% SRR) contact can be explained with the level of rubbing of surfaces involved due to sliding (Fig. 2). The level of sliding induces rubbing between tribo pair with increase in sliding velocity, which results an increase in friction. The blending of 0.4% (w/w) rGO registers minimum friction coefficient in both the cases.

3.3 Noise and Vibration

The overall noise and vibration level are suppressed by blending of rGO to the commercial lithium grease. These parameters were minimum for 0.4% (w/w) rGO in base grease.

The optimality of rGO concentration in grease can be explained with following arguments (i) at lower concentration there is a starvation of rGO into contact and (ii) at higher concentration, the rGO is present in the form of micro-agglomerates, which are not able to enter the contact zone.

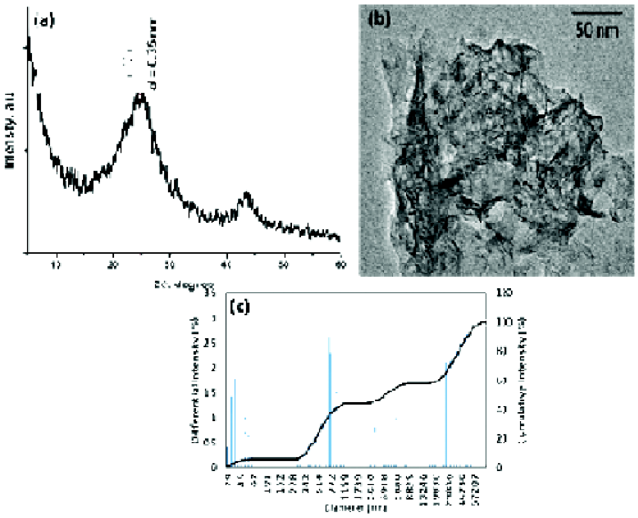

Fig. 1: (a) XRD pattern, (b) HRTEM and (c) DLS of rGO nano sheets in toluene.

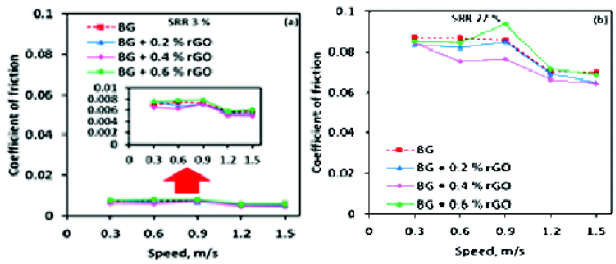

Fig. 2: Friction response of grease samples at point contact for (a) 3% SRR (b) 27% SRR.

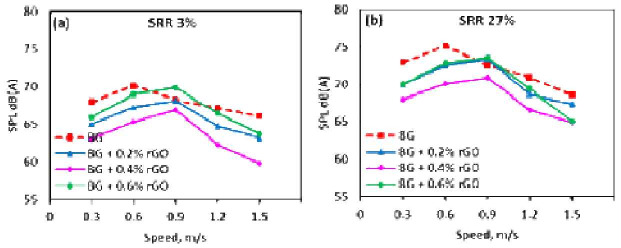

Fig. 3: Sound pressure levels in dB (A) for grease samples at (a) 3% SRR and (b) 27% SRR.

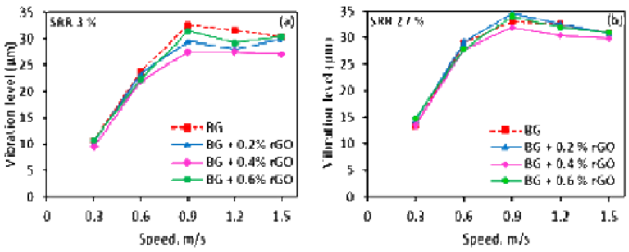

Fig. 4: Overall vibration levels in ¼m for grease samples at (a) 3% SRR and (b) 27% SRR.

4. CONCLUSION

Potential of rGO as additive to grease is explored and commercial grease is modified. The results show that the blending of optimum amount of rGO can improve the tribological, noise and vibration responses, all together. The blending of 0.4% (w/w) rGO to grease leads to almost 30% reduction in friction under both rolling and rolling coupled with sliding tribological contact. The friction seems to be controlled by the lamellar structure of the rGO and its concentration. At optimum concentration of rGO, overall noise and vibration level were also at their minima.

REERENCES

[1] T. Cousseau, M. Bjorling, B. Graca, A. Campos, J. Seabra, and R. Larsson, "Film thickness in a Ball-on-Disc Contact Lubricated with Greases , Bleed Oils and Base Oils," *Tribology International*, vol. 53, pp. 53–60, 2012.

[2] L. Huang, D. Guo, and W. Shizhu, "Film Thickness Decay and Replenishment in Point Contact Lubricated With Different Greases: A Study into Oil Bleeding and the Evolution of Lubricant Reservoir," *Tribology International*, vol. 93, pp. 620–627, 2014.

[3] A. Mohamed, T. A. S. Osman, A. A. Khattab, and M. Zaki, "Rheological Behavior of Carbon Nanotubes as an Additive on Lithium Grease," *Journal of Nanotechnology*, vol. 2013, pp. 1–4, 2013.

[4] Z. J. Zhang, D. Simionesie, and C. Schaschke, "Graphite and Hybrid Nanomaterials as Lubricant Additives," *Lubricants*, vol. 2, pp. 44–65, 2014.

[5] H. P. Mungse, O. P. Sharma, H. Sugimura, and O. P. Khatri, "Hydrothermal Deoxygenation of Graphene Oxide in Sub- and Supercritical 2014.

NUMERICAL MODELING OF 3D RANDOM GAUSSIAN ROUGH SURFACES

Deepak K. Prajapati[1] and Mayank Tiwari[2*]

[1, 2]Indian Institute of Technology, Patna, India, 801106
*mayankt@iitp.ac.in

KEY WORDS: surface topography parameters; summit identification method; Weibull distribution; Gaussian distribution

ABSTRACT

This work demonstrates the method for correct prediction of contact parameters by accounting the asymmetry in summit height. The contact parameters are calculated for high value of plasticity index. The Isotropic Gaussian rough surface is generated using 2D FIR (finite impulse response) technique with fast Fourier transform. The spectral moment and summit identification (SID) methods are used to determine the summit parameters. On comparison, significant difference in summit parameters are found. The contact parameters (total real contact area and total normal load) for isotropic Gaussian surface are calculated assuming Gaussian and non-Gaussian distribution of summit height. The results indicate that, asymmetry in summit height should be considered for correct prediction of contact parameters for isotropic Gaussian rough surfaces.

INTRODUCTION

Many engineered rough surface are random, anisotropic and non-Gaussian.But it is equally known that some machined rough surfaces are also isotropic and Gaussian. Previous reported works**[1-4]** showed that most of the effort has been made for characterization of rough surfaces, statistical and numerical contact modeling of rough surfaces. In all these reported works, numerical simulations are performed for very low value of plasticity index. High value of plasticity index is achieved in many tribological applications i.e. gears, cams, seals, rolling bearings, to name a few. Kogut and Etsion **[4]** developed a FEM based elastic-plastic model for rough surfaces. They increased the plasticity index up to 8 considering Gaussian distribution of asperity heights. The literature showed that, the elastic-plastic contact model of isotropic random Gaussian rough surface containing asymmetry in summit height for high value of plasticity index have not been reported earlier. In this work an attempt is made to fill this gap. The isotropic random Gaussian rough surface is generated using 2D filter technique, proposed by Hu and Tonder **[5]**. Summit (asperity) parameters are calculated and compared using both spectral moment and summit identification methods. To demonstrate the significance of asymmetry in summit height, a rough surface contact simulation is made for polysilicon surfaces. Normalized Weibull distribution is used to account the asymmetry in summit height. Contact parameters (real contact area, total normal load) are calculated for Weibull distribution of asperity heights and compared with those obtained by assuming Gaussian distribution of summit height.

METHODOLOGY

Numerical Generation of Rough Surface

The isotropic Gaussian rough surface is generated by using the method proposed by Hu and Tonder [5]. Overall procedure for generation of isotropic Gaussian rough surface can be summarized as follows:

1. Generate random input sequence of order N×M, η (I, J) which follows the properties of Gaussian distribution i.e. mean (m = 0), standard deviation (S_q =1 μm).

   where I = 0, 1, 2, 3, 4………N; J =0, 1, 2, 3, 4………M and N and M are total number of sampling points.

2. Specify the negative exponential form of autocorrelation function R_exp (k, l) [3].

$$R_{exp}(k,l) = \sigma^2 \times \exp\left[-2.3\left\{\left(\frac{k}{\beta_x}\right)^2 + \left(\frac{l}{\beta_y}\right)^2\right\}^{0.5}\right]$$

   where k = 0, 1, 2, 3, 4…………., N/2; l =0, 1, 2, 3, 4………, M/2; β_x and β_y are the correlation lengths in x and y direction respectively.

3. Obtain the power spectral density S_{exp} (ω_x, ω_y) of negative autocorrelation function by taking the inverse fast Fourier transform.

$$S_{exp}(\omega_x, \omega_y) = \frac{1}{nm}\sum_{k=-\frac{n}{2}+1}^{\frac{n}{2}-1}\sum_{l=-\frac{m}{2}+1}^{\frac{m}{2}-1} R_{exp}(k,l)\,e^{-jk\omega_x}e^{-jl\omega_y}$$

4. Obtain power spectral density by taking the fast Fourier transform (FFT) of a random input sequence η (I, J). Computational expression (in MATLAB 2014) for

obtaining the power spectral density can be expressed as follows:

$$S_\eta(\omega_x,\omega_y) = \text{abs}\ \ (\text{fftshift}\ \ (\text{fft2}\ (\eta(x,y)\times \text{conj.}\ (\text{fft2}\ \ (\eta(x,y)))\ )))\ /\ (N\times M)$$

where, S_η is spectral density of input sequence which will be a constant value (C) for a random sequence of a white noise type.

5. The filter function H (ω_x, ω_y) in frequency domain is generated by the formula.
6. The filter function in spatial domain is by taking the inverse fast Fourier transform of H (ω_x, ω_y).
7. The filter function h (k, l) and modified input sequence η(I, J), numerical rough surface can be generated by taking the convolution of η(I, J) and h (k, l).

$$H(\omega_x,\omega_y) = \sqrt{S_{exp}(\omega_x,\omega_y)/C}$$

Fig.1 Surface map of numerically simulated random isotropic Gaussian rough surface. The rough surface consists of 200 x 200 sampling point with 1im sampling interval in both x and y directions. The correlation lengths in both x and y directions are taken same ($\beta_x = \beta_y$ = 10μm) for getting the isotropic surface.

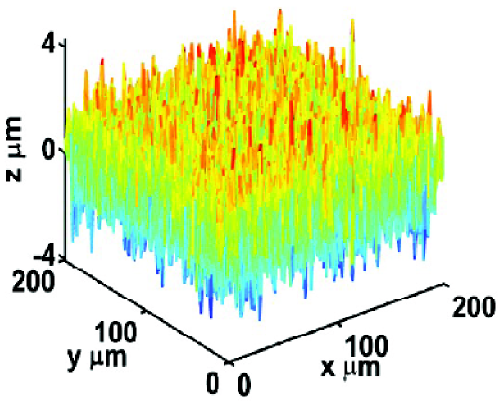

Fig. 1. Surface map of numerically simulatedisotropic Gaussian rough surfaces

CALCULATION OF SURFACE TOPOGRAPHY PARAMETERS

Summit Identification Method (SID): Surface topography parameters such as mean summit radius of curvature; summit density are two most important quantities extensively used for statistical contact modeling of rough surfaces [3]. In this work, surface topography parameters are calculated using summit identification (SID) method. Summit identification method is based on identifying the summits (asperities) with in nominal (sample) area (A_n). In this method, a summit is considered as local maxima with height greater than its eight nearest-neighbor point. Identifying all the summits (N_{sum}) in a nominal area, summit density ($\eta = N_{sum}/A_n$) can be obtained by dividing total number of summit to nominal area (sample area). To obtain summit radius of curvature (R), summit curvature for each ith summit is calculated in two orthogonal directions $\kappa_{x,i} = d^2z/dx^2$ and $\kappa_{y,i} = d^2z/dy^2$ using central finite difference formula and then, summit radius of curvature (R_i) of each summit 'i' can be obtained by taking the inverse mean of κ_{x1} and $\kappa_{y,1}$[3]. Mean summit radius of curvature is calculated by taking the arithmetic mean of all individual summit radii.

Spectral Moment Method: Calculation of spectral moments from power spectrum is difficult because correct estimation of lower and higher cut–off frequency is also difficult due to its dependency on sampling length and resolution of instruments. For digitized data of rough surface, center finite difference formula is another way to calculate spectral moments approximately [3]. Advantage of this method is due to its dependency on only two parameters namely (i) three adjacent value of surface heights (ii) sampling interval. In this work even order (m_0, m_2, m_4) spectral moments are calculated using center finite difference formula [3]. Spectral moments (m_0, m_2, m_4) are calculated over 200 cross sections in both the direction i.e. in x and y direction and average value of spectral moment is used in this work. For isotropic Gaussian rough surfaces, only three surface moments (m0, m2 and m4) are required to determine the surface topography parameters [3].

Equations for determining equivalent bandwidth parameter (α), mean summit curvature (κ_m) or summit radius of curvature ($R=1/\kappa_m$), skewness (σ_{sk}) of summit height [6] and standard deviation (σ_s) of summit height can be written as follows [3,6]:

$$\alpha = \frac{m_{00}m_4}{m_2^2}$$

$$\kappa_m = 1.5048\sqrt{m_4}\ ,\ 1/\mu m$$

$$\sigma_s^2 = \left(1 - \frac{0.8968}{\alpha}\right)m_{00}\ ,\mu m^2$$

$$\sigma_{sk} = \frac{0.2199}{(\alpha - 0.8968)^{3/2}}$$

Table 1 shows the comparison of surface topography parameters determined using both summit identification (SID) and spectral moment methods. The bandwidth parameters (α) is calculated by using expression, developed in Ref. [1]. It can be seen from Table 1 that there is asymmetry in summit height (σ_{sk} = 0.164), and it is necessary to include this asymmetry in contact modeling of Gaussian rough surfaces.

Table 1 Comparison of summit parameters calculated from spectral moment and SID methods

Parameters	SID method	Spectral moment method
η (1/μm^2)	5.61×10^{-2}	5.13×10^{-2}
σ_s (μm)	7.57×10^{-1}	7.87×10^{-1}
R (μm)	7.27×10^{-1}	6.09×10^{-1}
σ	3.635×10^{-2}	3.1×10^{-2}
σ_{sk}	1.64×10^{-1}	1.20×10^{-1}
β_{ku}	3.14	3.005
α	N/A	2.3909
Ψ	8	8

RESULTS AND DISCUSSION

To demonstrates the effect of asymmetry in summit (asperity) height, a contact rough surface simulation is performed by considering the properties (young modulus, poison ratio, hardness) of polysilicon surfaces [6]. The elastic-plastic rough surface contact model developed by Zhao et al. [2] is adopted for contact modeling. The equations for determining the real contact area and total normal load developed in Ref. [2] can be re-written as follows:

$$A_t^*=\pi\beta\int_{h^*-y_s^*}^{h^*-y_s^*+w_1^*} w^*\phi^*(z^*)\,dz^*+2\pi\beta\int_{h^*-y_s^*+\omega_2^*}^{\infty}\omega^*\phi^*(z^*)\,dz^*$$
$$+\pi\beta\int_{h^*-y_s^*+\omega_1^*}^{h^*-y_s^*+\omega_2^*}\left[1-2\left(\frac{\omega^*-\omega_1^*}{\omega_2^*-\omega_1^*}\right)^3+3\left(\frac{\omega^*-\omega_1^*}{\omega_2^*-\omega_1^*}\right)^2\right]\omega^*\phi^*(z^*)\,dz^*$$

$$W_t^*=\frac{4}{3}\beta\left(\frac{\sigma}{R}\right)^{1/2}\int_{h^*-y_s^*}^{h^*-y_s^*+w_1^*} w^{*3/2}\phi^*(z^*)\,dz^*+\frac{2\pi H\beta}{E}\int_{h^*-y_s^*+\omega_2^*}^{\infty}\omega^*\phi^*(z^*)\,dz^*$$
$$+\frac{\pi H\beta}{E}\int_{h^*-y_s^*+\omega_1^*}^{h^*-y_s^*+\omega_2^*}\left[1-\left(1-k\right)\frac{\ln\omega_2^*-\ln\omega^*}{\ln\omega_2^*-\ln\omega_1^*}\times\left(1-2\left(\frac{\omega^*-\omega_1^*}{\omega_2^*-\omega_1^*}\right)^3+3\left(\frac{\omega^*-\omega_1^*}{\omega_2^*-\omega_1^*}\right)^2\right)\right]\omega^*\phi^*(z^*)\,dz^*$$

where, $A^*_t = A_t/A_{nom}$ is the dimensionless total real contact area, $W^*_t = W_t/(EA_{nom})$ is the dimensionless total normal load carried by asperity, β is the constant which is product of summit density, summit radius of curvature and standard deviation of surface height, $\pi^*(z^*)$ the normalized distribution of summit heights, H is the hardness of material, h* is the normalized separation between mean of rough surface and rigid smooth plane, ω* is the normalized deformation of summit height, E is the equivalent Young modulus, A_{nom} is the nominal area of the surface, which is 200×200 μm^2 in this work. It should be noted that, all parameters are normalized with standard deviation of summit height (σ_s).

DISTRIBUTION OF SUMMIT HEIGHT

(i) Weibull distribution:

The expression for normalized Weibull distribution [6] used in this work for accounting the asymmetry in summit height, can be written as:

$$\varphi_W^*(z^*)=\beta_W\left(B_1+z^*\sqrt{B_2-B_1^2}\right)^{\beta_W-1}\sqrt{B_2-B_1^2}\,e^{-\left(B_1+z^*\sqrt{B_2-B_1^2}\right)^{\beta_W}}$$

where, B_n is the Gamma function can be written as:

$$B_n=\Gamma\left(1+\frac{n}{\beta_W}\right)$$

The skewness (σ_{sk}) of summit height is used to determine the β_w.

$$\sigma_{sk}=\frac{B_3-3B_2B_1+2B_1^3}{\left(B_2-B_1^2\right)^{1.5}}$$

(i) Gaussian distribution

For comparison purpose, the contact parameters are calculated assuming Gaussian distribution of summit height. The expression for normalized Gaussian distribution can be written as:

$$\varphi_G^*(z^*)=\frac{1}{\sqrt{2\pi}}\exp\left(-0.5z^{*2}\right)$$

Fig. 2 shows the non-dimensional load variation with normalized surface separation (h^*). It can be seen that, load carried by asperity increases with decrease in surface separation. As the surface separation decreases, more number of asperity coming into contact which required higher load to deform the asperities. The difference in prediction of total normal load assuming Gaussian and Weibull distribution of asperity height can be also seen from Fig. 2. For a particular value of surface separation, total normal load required for deformation of asperities is higher for Weibull case.

Fig. 3 shows variation of total real contact area (A^*) with normalized surface separation (h^*). From Fig.3 it can be seen that, real contact area decreases with increase in surface separation. For a particular value of surface separation, predicted total real contact area is higher for Weibull distribution.

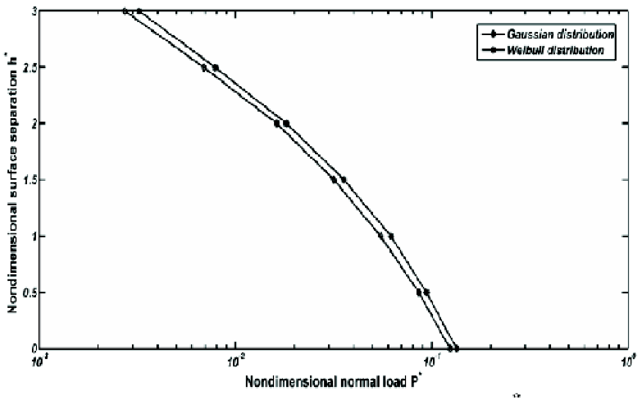

Fig. 2. Variation of non-dimensional load (P^*) with surface separation (h^*)

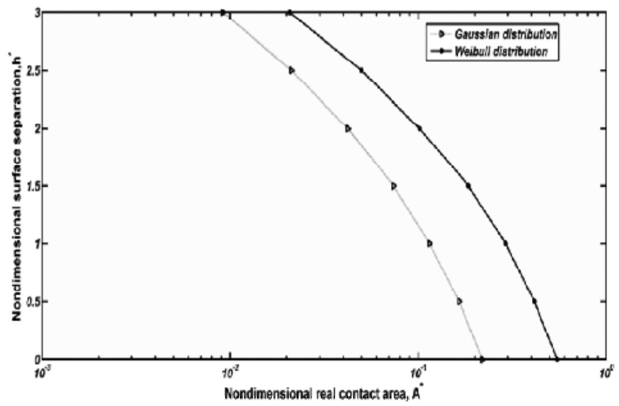

Fig. 3. variation of non-dimensional real contact area (A^*) with surface separation (h^*)

OBSERVATIONS

In this work, new results are presented considering SID with Weibull distribution of asperity heights for high value of plasticity (Ψ = 8) index which was not discussed in Ref. [4]. It can be seen from Fig. 2 that; total normal contact load is higher for a particular value of surface separation (h^*) considering asymmetry (Weibull distribution) in asperity heights. Fig. 3 presents variation of non-dimensional real contact area with normalized surface separation (h^*) for high value of plasticity index Ψ=8, considering both Gaussian and Weibull distribution of asperity heights. Large real contact area obtained for Weibull distribution of asperity heights resulting in lower the contact stress between asperities and rigid flat. From this work, it is clear that asymmetry in asperity heights should be considered even for random isotropic Gaussian surface for obtaining the better results as obtained with assuming Gaussian distribution of asperity height.

REFERENCES

[1] Nayak, P.R. Random process model of rough surface. Transactions of ASME Journal of Lubrication technology,1971, pp. 398-407.

[2] Zhao, Y., and Chang, L. A model of asperity interactions in elastic plastic contact of rough surfaces. ASME Journal of Tribology, 2000, Vol. 123, pp.857-864.

[3] Pawar, G., Pawlus, P., and Etsion, I. The effect of determining topography parameters on analyzing elastic contact between isotropic rough surfaces. ASME Journal of Tribology, 2013, Vol.135, pp.1-10.

[4] Kogut, L., and Etsion, I.A finite element basedelastic-plastic model for the contact of rough surfaces. Tribology Transactions, 2010, Vol. 46, pp. 383-390.

[5] Hu, Y. Z., and Tonder, K. Simulation of 3-d random surface by 2-d digital filter and Fourier analysis. Int. J. Mech. Tools Manufac., 1992, Vol. 32, pp. 83-90.

[6] Yu, N., and Polycarpou, A. A. Extracting summit roughness parameters from random Gaussian surfaces accounting for asymmetry of the summit heights. ASME Journal of Tribology, 2004, Vol. 126, pp.761-766.

ON THE PERFORMANCE OF HYDRODYNAMIC STEP SLIDER BEARING WITH SURFACE TEXTURE

Shakti Ranjan Naik[1] and Ram Turaga[2]
[1)]Department of Civil Engineering, Indian Institute of Technology Madras, Chennai, 600 036, INDIA,
[2)]Office of Development and Alumni Affairs, Indian Institute of Science, Bangalore 560 012, INDIA.
[*]Corresponding e-mail: ramturaga2@gmail.com

KEY WORDS: hydrodynamic step slider bearing; surface texture; CFD

ABSTRACT

The influence of surface texture geometry on the steady state characteristics of hydrodynamic step-slider bearing has been investigated. A single dimple located on the stationary surface of the finite step-slider bearing has been considered. Three cases of dimple locationnamely the lower step, higher step and on both steps have been studied. Both negative (recessed) and positive (protruding) dimples have been considered. The dimple geometries modeled are rectangle, Triangle and Trapezoid. The parameters considered are dimple depth to film thickness ratio, distance of the dimple from the nearest edge along its length to the length of the dimple, distance of the dimple from the nearest edge along its width to the width of the dimple and density ratio (area of dimples to the total pad area). The governing Navier-Stokes equations considering incompressible fluid for an isothermal case have been solved by the finite volume method using ANSYS FLUENT. The load carrying capacity, friction force and coefficient of friction have been calculated and normalized with smooth case. It has been observed that a negative dimple on the lower step results in a reduction in the coefficient of friction whereas a positive dimple on the higher step gives significant reduction in coefficient of friction of the bearing. The magnitude of reduction in coefficient of friction is not uniform and varies with the texture geometry, texture density and film thickness ratio.

INTRODUCTION

Surfaces with textures also called as dimples on a stationary surface of a bearing have shown to generate pressure and carry load. These textures have shown to reduce coefficient of friction. Textures can be created using lasers, chemical etching and machining **[1].** The encouraging results led to further studies by creating textures on surfaces of face seals to minimize leakage and friction, in piston rings of internal combustion engines to reduce friction and thrust bearings to increase load carrying capacity and step slider bearing's **[1-4]**. Experimental and CFD studies on performance of thrust bearings with textures have been reported **[5,6].** In a CFD study the influence of surface texture geometries on the stationary surfaces of a step slider hydrodynamic bearing was performed to determine the steady state characteristics of the bearing. The open pocket texture on the bearing surface was found to give higher load carrying capacity**[6].**

In this study the influence of surface texture on the performance of step slider bearing has been done by solving the Navier-stokes equations using computational fluid dynamics method (CFD). The CFD based modeling approach provides us with a detailed information on the bearing texture region which would not have been obtained by the solution of Reynolds Equation. The steady state properties of the step-slider bearing have been evaluated. Different texture geometries have been created on the stationary bearing surface to evaluate their influence on the reduction of coefficient of friction.

METHODOLOGY

Governing Equations:

Considering the flow to be laminar and assuming isothermal conditions, the mass conservation and momentum equations can be written as **[6].**

$$\nabla \,.\, V = 0 \tag{1}$$

$$V.\nabla V = \tfrac{1}{\rho}\Delta P + \tfrac{\mu}{\rho}\nabla^2 V \quad (2) \tag{2}$$

where V is the velocity vector, P the static pressure, ρ the fluid density and μ the viscosity. The above equations (1) and (2) are solved using the finite volume method with the second order scheme as adopted by commercial package ANSYS-FLUENT as described in **[6].**

Geometries, Boundary Conditions and Parameters Studied:

A typical Step slider bearing considered in this study is as shown in Fig. 1. The smooth bearing geometry data for step slider bearing used is from earlier reported work **[7, 8]**.

The surface texture consists of a single dimple of rectangular, triangular, trapezoidal geometries on either the lower step or the top step and both the steps. Both positive and negative dimples are considered in this study. Positive dimples are protrusions on the surface whereas the negative dimples are recesses. A typical step slider bearing with negative dimple is shown in Fig. 2 and with positive dimple in Fig. 3. The geometries considered in this study are rectangular, triangular and trapezoidal are shown in Fig. 5.

Simulations have been done for different dimpledepths and the maximum depth considered is limited to less than twice the minimum film thickness. The texture density, defined as the area of the texture to the pad area, is varied between 4.75% and 11%. The texture density is varied by changing two parameters (zeta and beta). Zeta is the length ratio and beta is the width ratio. The length ratio is defined as the ratio of distance of the dimple from the edge of the bearing in length direction to the length of the dimple. The width ratio is defined as ratio of the distance of dimple from the edge of the bearing in width direction to the width of the bearing. A zeta and beta of 1 gives a density ratio of 11.11%. Similarly a zeta of 1 and beta of 2 results in a density ratio of 9.5% and a zeta of 1 and beta of 3 results in density ratio of 4.75%.

The bearing geometry has been meshed completely using Multi Zone hex mesh. The geometry can be subdivided for meshing into two parts, the step-slider bearing and the dimple. The edge meshing option has been used to mesh the step slider bearing and the dimple. The edges along the width have been divided into 200-250 number of divisions. The edges along the length have been divided independently till the step, thus the number of divisions for each step along the length is around 100-125. The thickness of the fluid at inlet is also meshed using the edge option with 10-15 number of divisions. This results in about 250 divisions along the length and breadth and 10-15 layers across the height. With these settings there are approximately 4,00,000-5,00,000 elements. A meshed step slider being is shown in Fig. 4. The bearing with dimple is meshed in a similar manner. Depending upon the geometry and the area density of the dimple, the number of divisions along its length, width and height are decided. About 50-75 number of divisions along the length and width and 4-6 number of divisions for the thickness of the dimple. The complete meshed model contains about 5,00,000-8,00,000 elements present in it.

A mesh independency study to find out the optimum number of elements required has been performed. This is done by plotting a graph between the load carrying capacity (W) versus the number of elements (N). In this study further refinement of mesh is limited when a change of less than 1% is seen in the load carrying capacity with the change in number of elements. For a smooth bearing it is observed to be about 4,50,000 elements and for bearing with dimple on the surface the number of elements are around 5,50,000.

The lubricant is assumed as incompressible and isothermal conditions have been considered. The lubricant pressure has been assumed to be higher than vapor pressure of the lubricant hence cavitation has not been considered.The pressures at the inlet and outlet boundaries of the bearing are set to atmospheric pressure.Half-Sommerfield type of boundary conditions for calculation of load capacity has been used and the negative pressures are made equal to zero **[6]**. At walls, no slip conditions are assumed. The pressure staggering option (PRESTO in FLUENT) is used for pressure calculation. The pressure distribution obtained by solving the governing equations is integrated to calculate the load carrying capacity. The friction force and coefficient force are also calculated.

Simulations have been done for different geometries and varying dimple depths. Results are plotted as load carrying capacity ratio (ratio of load carrying capacity of bearing with a dimple to the smooth case) with change in film thickness ratio (ratio of the dimple depth to the minimum film thickness). The corresponding friction force ratio and the coefficient of friction ratios are plotted with the variation in film thickness ratio.

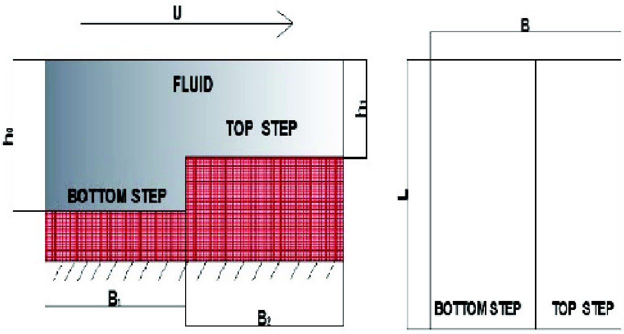

Fig 1: Geometry of the Step slider bearing

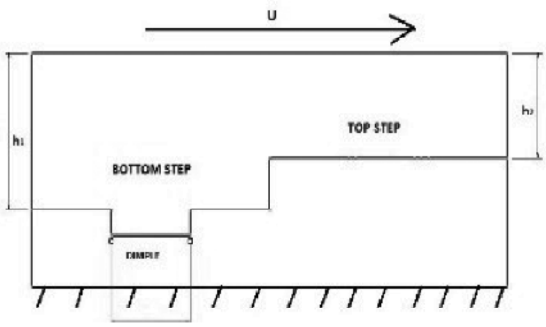

Fig 2: Geometry of step slider bearing with negative dimples

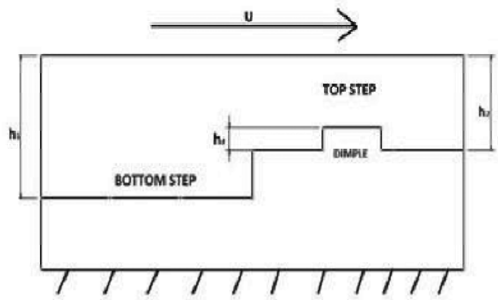

Fig 3: Geometry of step slider bearing with positive dimples

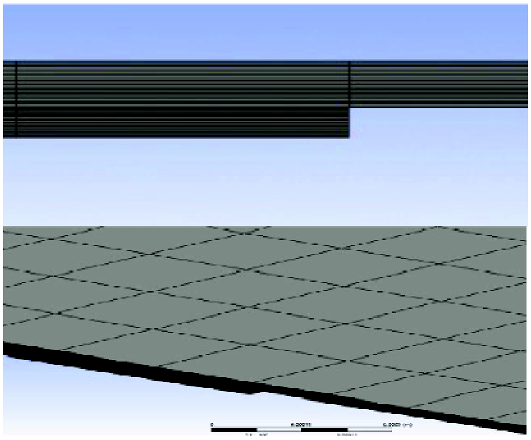

Fig. 4: Meshed Step Slider bearing

Table 1: Dimensions of step slider bearing [8]	
Length of bearing	50 mm
Width of bering	50 mm
Initial Step length	25 mm
Inlet film thickness	0.02-0.04 mm
Outlet film thickness	0.02 mm
Runner velocity	5 m/s
Viscosity	0.02 kg/m-s
Density of lubricant	900 kg/m^3

VALIDATION OF THE CFD MODEL

The validation of thesmooth case of Rayleigh step bearing model was done for two sliding velocities of 10m/s and 30m/s**[7]**. A typical mid plane pressure distribution obtained is shown in Fig 6. The maximum pressure compares within 1% of the reported results.

Using the data from Table 1full 3D CFD analysis has been performed. The load carrying capacity is plotted with variation in h1/h2 and b1/b2 as shown in Fig 7. This is done by a trial-error procedure to obtain the optimum height by fixing the minimum film thickness at outlet and varying the thickness at inlet. After fixing the height, the width ratio is varied to obtain the optimum bearing geometry based on maximum load carrying capacity.The optimum ratios thus obtained are h1/h2 =1.68 and b1/b2=1.26 as shown in Fig. 7. These two results are within 1.1% and 5% respectively of the reported results**[8]**.

RESULTS AND DISCUSSION

The dimple geometries have been created on the bearing geometry with optimum width ratio.A single dimple either negative or positive texture has been considered on the lower step, top step and both steps.

A typical 3-D pressure distribution and the pressure contour for a step slider bearing with rectangular dimple at the lower step is shown in Fig 8. The pressure distribution and contours for other geometries considered was similar in nature. However the magnitude of the maximum pressure varies.

The steady state characteristics of step-slider bearing with a rectangle dimple with varying density ratios are shown in Fig. 9. The load carrying capacity increases up to a film thickness ratio of 0.4, correspondingly the friction force ratio decreases and consequently the coefficient of friction decreases by about 1.1% compared to the smooth case.

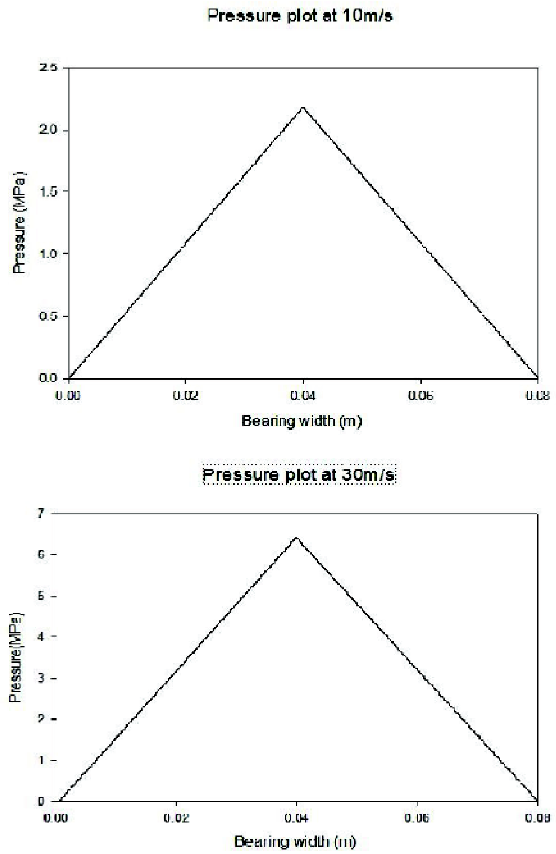

***Fig 6**: Mid Plane pressure distribution of smooth step slider bearing at 10 m/s and 30 m/s*

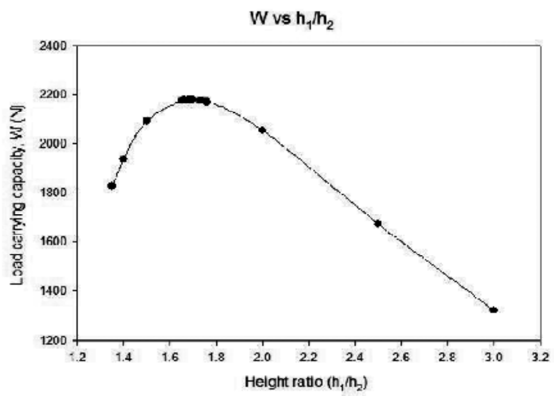

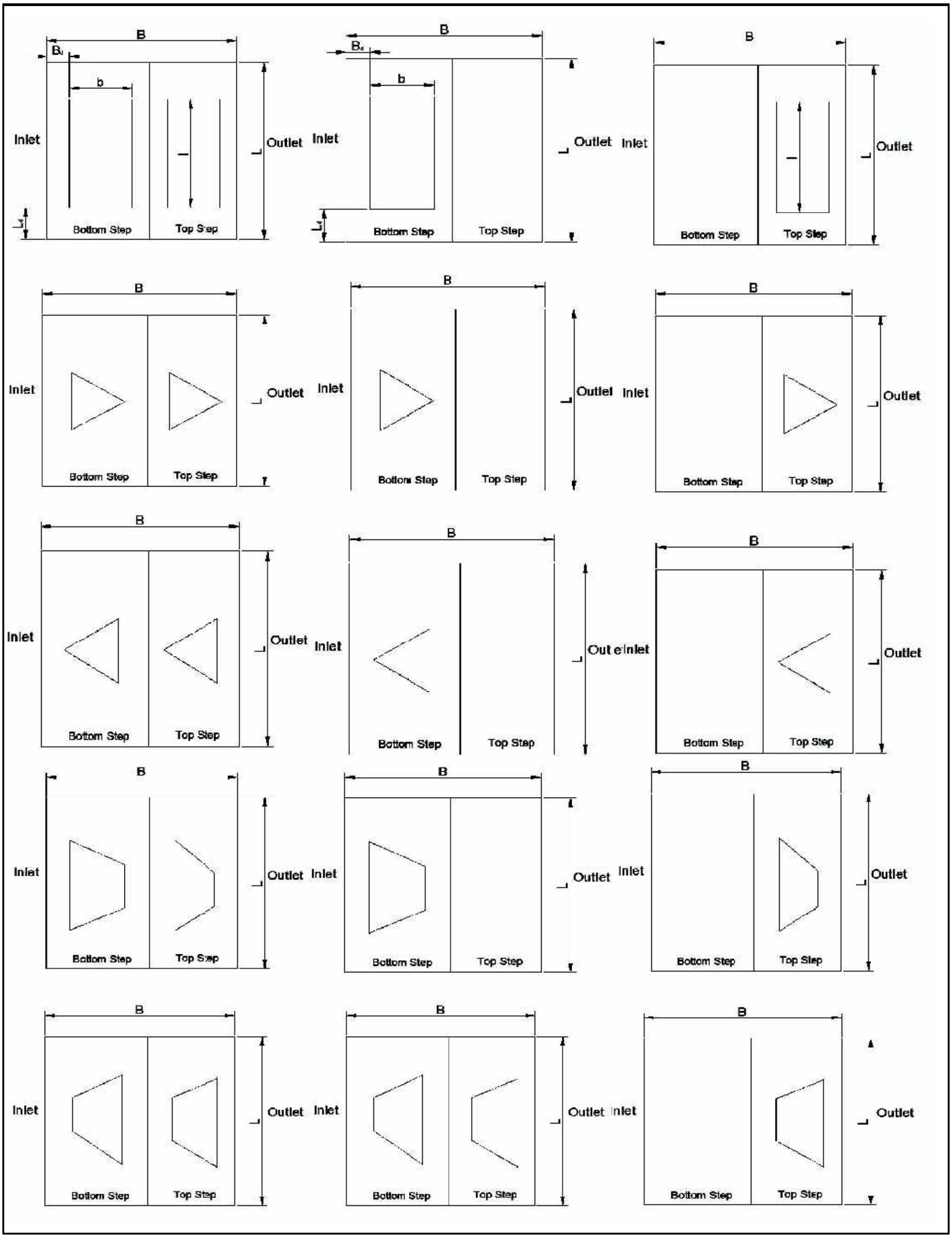

Fig. 5: Step slider bearing with dimples - The dimple orientations considered in the study for negative and positve dimples

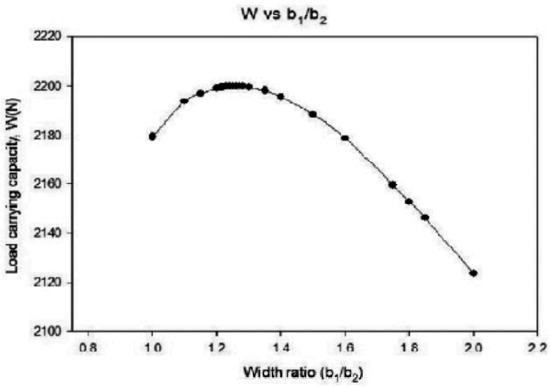

Fig 7: (a) Load capacity vs Height ratio, (b) Load capacity vs Width ratio for Smooth Bearing

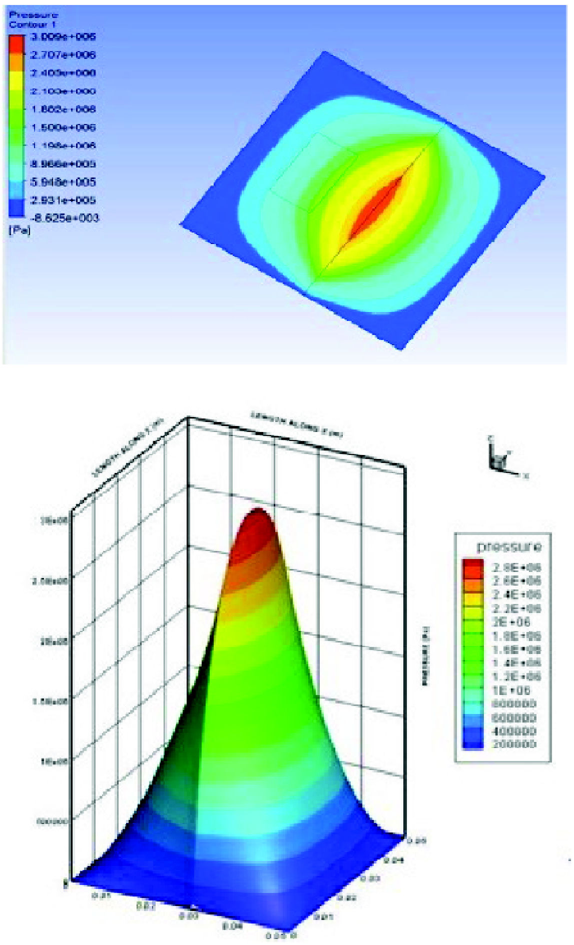

***Fig 8**: Pressure contour, 3-D pressure distribution of step slider with a rectangular dimple on lower step*

In case of the trapezoidal dimple with the smaller base facing outlet and an area density of 11% on lower step demonstrated a reduction of coefficient of friction of about 1.76% and an increase in load carrying capacity by 1.53% at film thickness ratio of 0.4. In the triangular dimple with its base facing outlet on lower step with a film thickness ratio of 0.4 and at the area density of 11.11%, a reduction in coefficient of friction by 1.70% was observed. For the trapezoidal dimple with smaller base facing inlet on lower step and at the same film thickness ratio and area density, the coefficient of friction dropped by 1.52% and the load carrying capacity increased by 1.28%. Slight increase in load carrying capacity and drop in coefficient of friction was noted for triangular dimple with its base facing inlet on lower step at same film thickness ratio and area density.

Of all the geometries considered, rectangular dimple on lower step demonstrated a greater reduction in coefficient of friction of about 1.7% with significant increase in the load carrying capacity of 1.55% at the film thickness ratio of 0.4 and area density of 11.11%.

The reduction in the Coefficient of friction is primarily due to the increase in the load carrying capacity and also due to reduction in the friction force compared to the smooth case. The dimples with higher density ratio show a greater influence on reduction in coefficient of friction**[9].**

The decrease in load carrying capacity ratio after film thickness ratio of 0.4 can be explained by studying the velocity vectors in the negative dimple located on lower step. It is observed that a strong flow recirculation occurs at film thickness ratio greater than 0.4 (Fig. 10).This contributes to reduction in the pressure generated and hence the load carrying capacity. This observation is in line with earlier reported studies**[10,11].**

In case of negative dimples at top step and both steps of the step slider the load carrying capacity decreases and the friction force increases. As a result the coefficient of friction increases.This behavior could be due to a flow reversal observed on the bottom step which causes a drop in pressure, thus decreasing the load carrying capacity. The flow recirculation observed in Fig 10 is also observed for bearing with surface textures on both the steps.

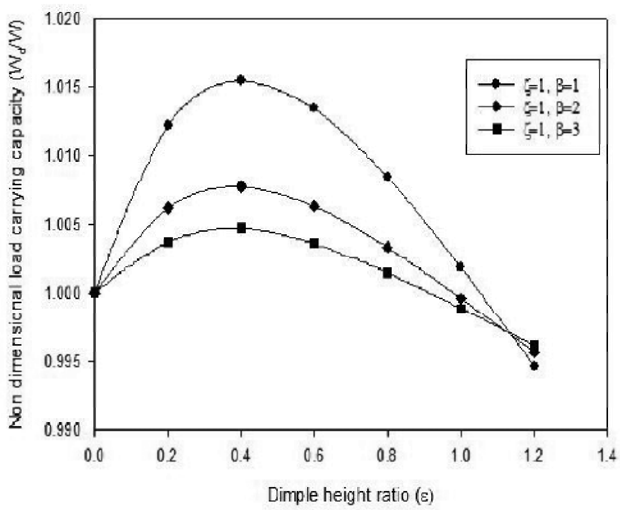

(a)

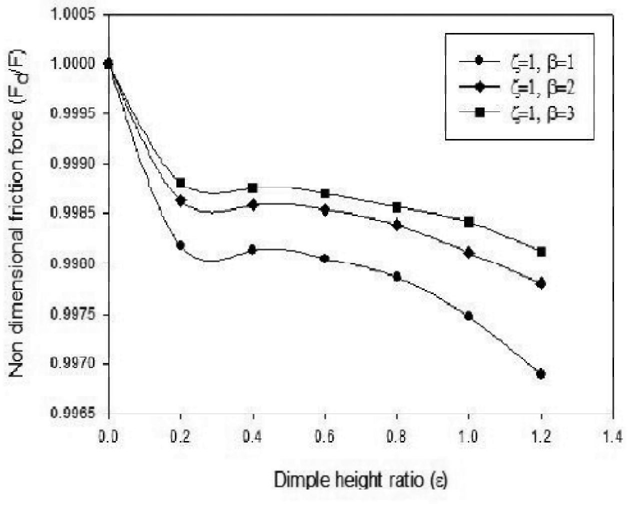

(b)

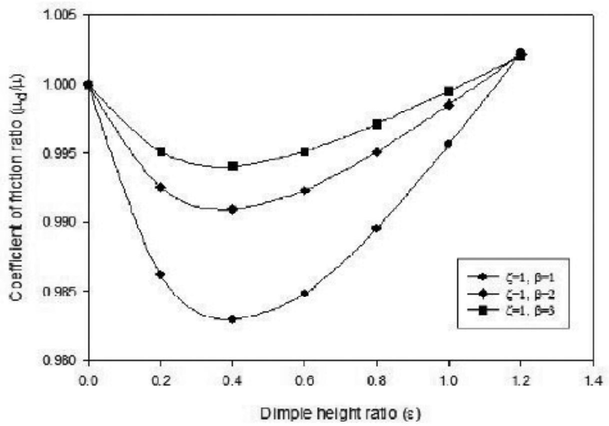

(c)

***Fig 9**: Non dimensional parameter versus film thickness ratio – negative rectangle dimple on bottom step*

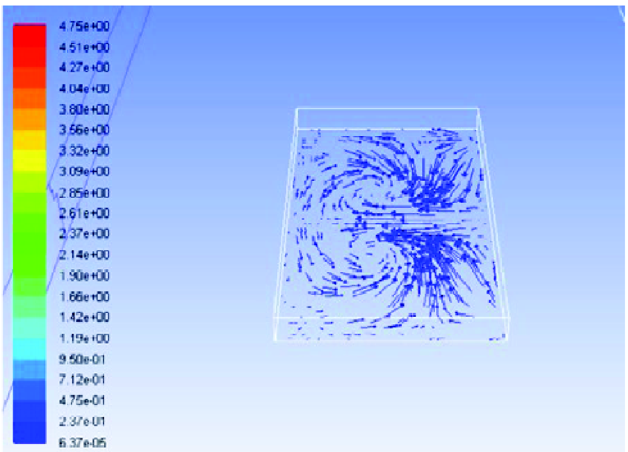

***Fig 10**: Velocity vectors - negative rectangular dimple on the bottom step.*

In case of step slider bearing with positive dimple on top step significant improvement in load carrying capacity has been found. A typical 3-D pressure distribution with contours for positive triangle dimple with base facing outlet located on the top step is shown in Fig 11. There is a significant increase in the load carrying capacity due to increase in the peak pressure. However at the exit region negative pressures were observed. These have been equated to zero while calculating the load carrying capacityas explained in literature **[6].** Negative pressures are however not observed for positive dimples on lower step and also when the dimples are located on bothbottom and top steps.

In case of a triangular dimple with base facing the outlet, the reduction in coefficient of friction is about 23% at a film thickness ratio of 0.75 and area density of 11.11%. At a film thickness ratio of 0.625 and area density of 4.75, the rectangular dimple on top step demonstrates a reduction of coefficient of friction of 17.85%. At a film thickness ratio of 0.75 and area density of 11.11%, the trapezoidal dimple with smaller base facing inlet on top step reduces the coefficient of friction by 15.71%. At same film thickness ratio, area density and location, trapezoidal dimple with smaller base facing outlet reduces the coefficient of friction by 11.67%. The triangular dimple with base facing inlet on top step at a film thickness ratio of 0.75 and area density of 4.75% reduces the coefficient of friction by 6.75%.

The increase in load carrying capacity in positive dimples on top surface could be due to their location being close to the maximum pressure region as has been reported in earlier studies **[10].** We also observethe magnitude of increase in load carrying capacity and friction force varies with film thickness height. This causes the coefficient of friction to have a maximum and a minimum point as shown in Fig 12(c).At higher film thickness ratio there is flow reversaland increase in shear stress.

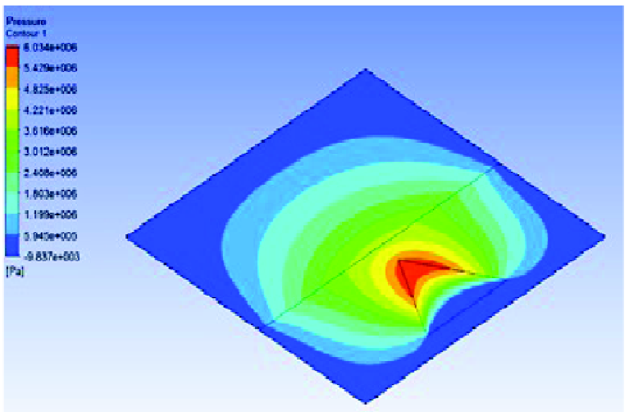

(a)

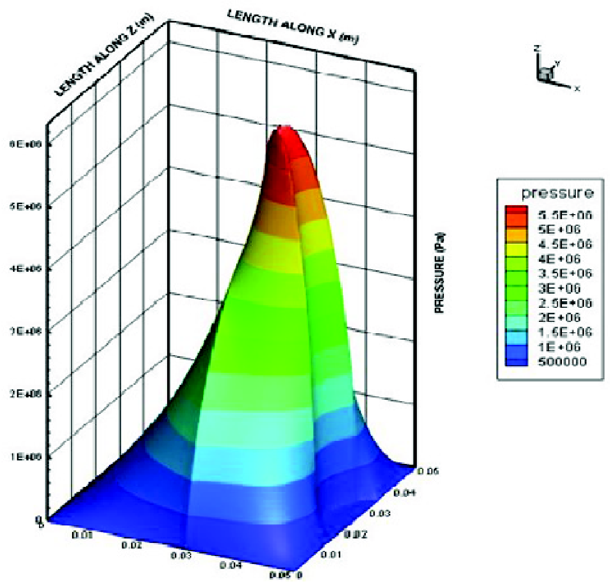

(b)

***Fig 11**: Pressure distribution of Positive Triangular Dimple on Top surface (a) pressure contours (b) 3-D pressure curve*

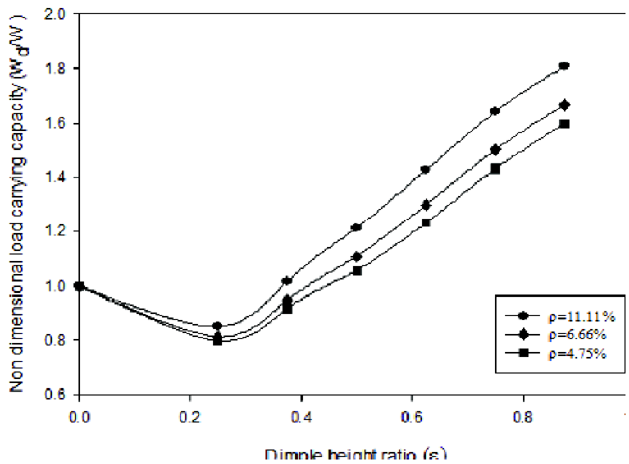

(a)

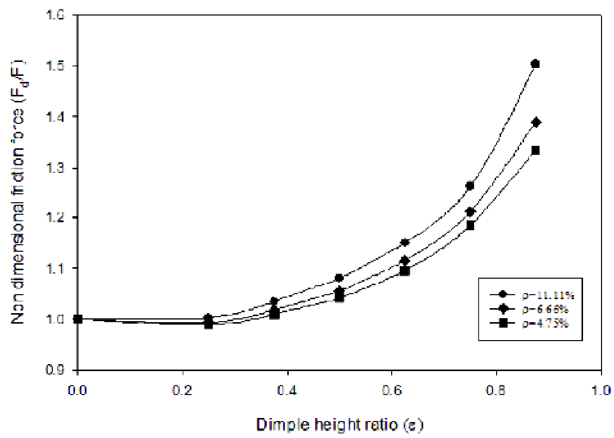

(b)

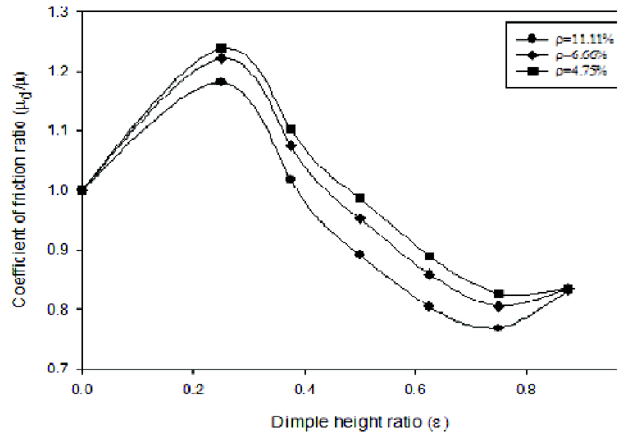

(c)

***Fig 12**: Non dimensional parameters vs film thickness ratio – Positive triangular dimple with base facing outlet on top step*

CONCLUSION

Presence of dimples on the surface of the step slider bearing has influence on the steady state characteristics of the bearing. The change in coefficient of (increase or decrease) depends on the geometry type, the density of the dimple, dimple geometry orientation and the film thickness ratio. A reduction in coefficient of friction is observed when using a negative dimple on the lower step and a positive dimple on the top step of the step slider bearing. Negative rectangular dimple on bottom step and positive triangle dimple with base facing outlet on top steps exhibit the highest reduction in coefficient of friction.

ACKNOWLEDGEMENT

This study was in part supported by a project grant received from the University Grants Commission, New Delhi during the second authors stay at GITAM University. The authors thank T. Vishak of ANSYS for his help with the use of ANSYS FLUENT Software.

REFERENCES

[1] IzhakEtsion. State of the art in laser surface texturing, ASME Journal of Tribology, 2005, 127, 248-253.

[2] Brixmer,V., Kligerman,Y., and Etsion, I., A Laser Surface Textured Parallel Thrust Bearing, STLE Tribology Transactions, 2003, 46(3), 397-403.

[3] Kligerman, Y., Etsion, I., Shinkarenko,A., Improving Tribological Performance of Piston Rings by Partial Surface Texturing, ASME Journal of Tribology, 2005, 127, 632-638.

[4] Victor Gabriel Marian, et. al., Theoretical and experimental Analysis of a Laser Textured Thrust Bearing, Tribology Letters, 2011, 44, 335- 343.

[5] Henry, Y., Bouye R, J. and Fillon, M., An Experimental Analysis of the hydrodynamic contribution of textured

thrust bearings during steady-state operation: A comparison with the un textured parallel surface configuration, Proc. IMechE Part J: Journal of Engineering Tribology, 2015, 229(4), 362-375.

[6] Dimitrios, G., and Foufilas et. al., Performance comparison between textured, pocket, and taper-land sector-pad thrust bearing using computational fluid dynamics thermo hydrodynamic analysis, Proc. IMechE Part J: Journal of Engineering Tribology, 2015, 229(4), 376-397.

[7] Dobrica, M., and Fillon, M., Reynolds Model Suitability in Simulating Rayleigh Step Bearing Thermo hydrodynamic Problems, STLE Tribology Transactions, 2005, 48, 522-530.

[8] Booker, J.F. and Huebner, K.H., Application of Finite Element Methods to Lubrication: An Engineering Approach, ASME Journal of Tribology, 1972, 313-322.

[9] Mihai B.Dobrica, et.al; Texturing Effects in Plane-Inclined Slider Bearings, Proceedings of the STLE/ ASME IJCT 2007-44258, October 22-24, 2007, San Diego, California, USA.

[10] Cupillard, S. et. al., Pressure Buildup Mechanism in a Textured Inlet of a Hydrodynamic Contact, ASME Journal of Tribology, 2008, 130.

[11] Jing Han, Liang Fang, Jiapeng Sun and Shirong Ge. Hydrodynamic Lubrication of Micro dimple Textured Surface Using Three-Dimensional CFD, STLE Tribology Transactions., 2010; 53:860-870.

A STUDY ON TRIBOLOGICAL PROPERTIES OF MIXTURE OF FATTY ACID METHYL ESTER (FAME) DERIVED FROM VARIOUS VEGETABLE OILS

S K Senapati[1*], B P Mishra[2] & S K Biswal[3]

[1]Indian Oil Corporation Ltd, Bhubaneswar Laboratory and Research Scholar of CUTM, jatni, Odisha
[2]School of Engineering, Centurion University of Technology and Management, Paralakhemundi, Odisha
[3]School of Applied Sciences, Centurion University of Technology and Management, Jatni, Odisha
*Corresponding author E-mail: senapatis@indianoil.in

Keywords: FAME, Biodiesel, HFRR, wear scar

ABSTRACT

Biodiesel, defined as the mono-alkyl esters of vegetable oils or animal fats, is an “alternative” diesel fuel that is becoming accepted in a steadily growing number of countries around the world. Since the source of biodiesel varies with the location, it is important to possess data on how the various fatty acid profiles of the different sources can influence biodiesel fuel properties. The properties of the various individual fatty esters that comprise biodiesel determine the overall fuel properties of the biodiesel fuel. In turn, the properties of the various fatty esters are determined by the structural features of the fatty acid and the alcohol moieties that comprise a fatty ester. Structural features that influence the physical and fuel properties of a fatty ester molecule are chain length, degree of un-saturation, and branching of the chain [10].

The aim of this work is to study the use of Biodiesel derived from various oil seeds of different fatty acid composition. The Palm Oil, Soybean Oil and Dillo Oil (Calophyllum Inophyllum) taken for this study. The biodiesel synthesized from these oils by transesterification reaction are mixed in different doses with mineral Diesel oil of BS IV and studied for physico-chemical properties as well as their lubricity properties in High Frequency Reciprocating Rig (HFRR) as per international standard test Method. The availability of these edible & non-edible seeds alone is not enough to fulfil the biodiesel demand of the country. From this study, the mixture of biodiesels from various oil seeds is a suitable option to meet the biodiesel demand of Country.

INTRODUCTION

Biodiesel is a renewable biofuel that is a viable alternative to fossil diesel. Its use has several environmental benefits related to the decrease of CO_2 emissions as well as several other air pollutants such as particulate matter, carbon monoxide, sulphur and polycyclic aromatic hydrocarbons. Biodiesel is mainly produced by a trans-esterification reaction where the oils or fats react with a short chain alcohol, usually methanol, in the presence of a homogeneous basic catalyst.

With the adoption of hydrodesulfurization (DHDS) process in oil refineries for reduction of total sulphur content in diesel fuel as per auto fuel policy, the diesel fuel loses its inherent lubricity, however certain amount of lubricity of diesel fuel is needed to save .

Several engine components from wear and failure. Though the loss of lubricity of the diesel fuel is observed with the removal of sulfur, it is mainly due to the loss of nitrogen and oxygen based polar trace compounds which are also removed in the DHDS process. All diesel fuel injection equipment has some reliance on diesel fuel as a lubricant. The lubricating properties of diesel fuel are important, especially for rotary and distributor type fuel injection pumps. Low lubricity fuel may cause high wear and scarring and high lubricity fuel may provide reduced wear and longer component life. Therefore, the lubricity of diesel fuel can vary dramatically. It is dependent on a wide variety of factors, which include the crude oil source from which the fuel was produced, the refining processes used to produce the fuel, how the fuel has been handled throughout the distribution chain, and the inclusion of lubricity enhancing additives whether alone or in a package with other performance enhancing additives.

The addition of biodiesel, even in very small quantities, has been shown to provide increases in fuel lubricity using a variety of bench scale test methods. The High Frequency Reciprocating Rig (HFRR) is commonly used for both the neat fuels and with fuels containing biodiesel.

In this study, biodiesel blends tested by high-frequency reciprocating rig (HFRR) for wear scar dia in mm. This study found that the biodiesel blends up to 20% with the diesel fuel (BS-IV) can effectively reduces both the wear of the tribo-contact surfaces as well as the friction coefficient in HFRR. These test results also showed a significant improvement in lubricity when adding mixture of three biodiesels (Palm oil, Soybean oil and Dillo oil) in the ratios of 5%,10% and 20% in BS-IV Diesel Fuel in comparison to individual FAME of particular oil.

MATERIALS

Fatty acid methyl ester of Palm, Soya and Dilo oils were prepared by base-catalyzed transesterification with methanol in the presence of NaOH as catalyst with constant stirring at 60C for 1hr duration. These Biodiesels (FAME) were designated here as SOME (Soybean oil methyl ester), POME (Palm oil methyl ester) and DOME (Dillo oil methyl ester) and tested for various physico-chemical properties as per standard test methods.

Table-1: Typical test results of raw vegetable oils

S.No.	Properties	Soybean Oil	Palm Oil	Dillo Oil
1.	Appearance	Clear yellow liquid	Clear yellow liquid	Dark green liquid
2.	Density @15°C, g/cc	0.910	0.913	0.916
3.	Kin.Viscosity @40C,cSt	35.60	40.45	33.2
4.	Kin.Viscosity @100C,cSt	8.27	9.41	7.76
5.	Viscosity Index (VI)	219	225	216
6.	Toatal Acid No.(TAN), mgKOH/g	0.40	0.10	10.3
7.	Saponification Value, mg KOH/g	189	197	190
8.	Pour Point,C	-9	+9	+6
9.	Flash Point	240	248	223
10.	Iodine value	127	52.4	84

Table-2: Fatty acid composition of vegetable oils

Fatty acids	Acronym	Soybean oil	Palm oil	Dillo Oil
Palmitic	16:0	11.0	43.5	15.3
Stearic	18:0	4.0	5.5	15.3
Oleic	18:1	23.0	40.5	35.7
linoleic	18:2	53.0	9.5	32.0
linolenic	18:3	9.0	1.0	1.7

Table-4: Test results of Biodiesel blends

Properties	Biodiesel blends						
Blend No.	1	5	6	7	8	9	10
Density 15°C	826.7	828.7	829.0	829.3	829.0	829.7	830.0
KV@40°C,	2.852	3.461	3.688	3.798	3.279	3.422	3.707
Flash pt,°C	45.5	47.0	48.0	48.5	47.5	48.5	50.5
Sulphur, ppm	41	39	38	40	38	39	34

Table-3: Typical test results of B100 (Biodiesel)

Properties	IS:15607-2016	SOME	POME	DOME
Appearance & color	C&B	C&B	C&B	C&B
Density@15°C,g/cc	0.860-0.900	0.870	0.875	0.880
Kin. Viscosity @ 40°C,c St	3.5 – 5.0	4.752	4.649	4.795
Acid Value. mgKOH/g, Max.	0.50	0.15	0.22	0.28
Water content, mg/kg, Max.	500	110	105	120
Ester content,% by mass, Min.	96.5	97.5	97.8	96.8
Free Glycerol, % by mass, Max.	0.02	0.012	0.014	0.018
Total Glycerol, % by mass, Max.	0.25	0.03	0.05	0.10
Pour Point, C	To report	-6	6	-6
Flash Point, °C Min.	101	164	172	174

EXPERIMENTAL

Lubricity test of esters and various blends were tested by High-Frequency Reciprocating Rig (HFRR) as per ISO 12156 at IOC, R&D. The BS-IV HSD of Panipat Refinery is taken for the experiments in this study. HFRR Test carried out for SOME, POME & DOME in the doses of 5% in BS-IV Diesel Fuel individually (designated as blend No.6,7 & 8) and Blend of above three FAME mixtures prepared in equal ratios and from this, the doses of 5%, 10% and 20% of mixture FAMEs (designated as blend No. 8, 9&10) blended with BS-IV Diesel Fuel.

The HFRR test is a computer-controlled reciprocating friction and wears test system. The HFRR test consists of a ball that is placed on a flat surface. Sample is put into

Fig-1: HFRR testing instrument

experimental place at 60C temperature. Steel ball is placed on a holder which is vertically tightly and then it is pressed on flat surface which is fixed horizontally with applying load. While contact surface is completely submerged into the fluid. The ball is then vibrated rapidly back and forth using a 1-mm stroke while a 200-g mass is applied for 75 minutes. HFRR testing was performed at Tribology department of IOC, R&D.

Kinematic Viscosity:

Viscosity is directly related to the atomization, lubricity, impinging distance, and burning efficiency of a liquid fuel. Biodiesel generally has a higher viscosity than petro-diesel, and thus has inferior atomization and spray, resulting in a larger mean liquid droplet diameter and a longer ignition delay. Figure 2 shows that the kinematic viscosity of the biodiesel samples at 40°C is determined and the blends of biodiesels in different ratios are within the limit of standard specification D6751. The KV@40°C of individual FAMEs are also within the specification limit of IS 15607-2016 standard.

It is observed, that the greater FAME conversion corresponds to a lower viscosity. However the viscosity of each methyl esters is higher than petrodiesel and their blends with petrodiesel increases to little extent, but remains within limit of IS: 16531-2016 specification

Ester Content:

Ester content is a measure of transesterification reaction completion. A higher conversion of triglycerides into methyl esters leads to a better engine performance. Ester content of biodiesel can vary greatly depending on the different technologies used and the raw materials available. Indian biodiesel standard, IS 15607-2016, sets a limit for the ester content of at least 96.5% while the American standard for biodiesel, ASTM D 6751does not specify a minimum for the ester content [8]. The ester content determined for the biodiesel obtained by alkali methanolysis of Soybean Oil, Palm Oil and Dillo Oil was determined by gas chromatography. The resulted data were processed, yielding a value of more than 96.5% ester content, indicating an almost complete conversion of triglycerides into methyl esters. Also free and total glycerin contents are within the specification limit values. Interference of free fatty acids and un-reacted glycerides contributes to better lubricity over neat esters due to their polarity-imparting oxygen atom, but have negative effect on engine performance. That's why, the estimation of free fatty acid and free glyceride contents essential before lubricity test by HFRR.

Flash Point:

The flash point determines the flammability of the material. In general, the flash point value specified by the quality standards is relatively high, for safety reasons regarding storage and transport and also to ensure that the alcohol is removed from the finished product. Low flash points may indicate alcohol residue in biodiesel. Studies in literature have shown that a methanol content of only 1% biodiesel can reduce the flash point of 170°C to less than 40°C. Thus, by introducing a quality specification of minimum flash point of 101°C, the Indian standard 15607:2016 implicitly limits the amount of alcohol at a very low value (<0.05%). Indian biodiesel standard, IS 15607:2016, sets a minimum limit for the flash point of 101°C while the American standard for biodiesel, ASTM D 6751, sets a minimum limit for the flash point of 130°C. Alcohol can also affect fuel pumps, seals, elastomers, and can result in poor combustion properties. The flash point for the biodiesel obtained by alkali methanolysis of Soybean, Palm and Dillo oils were more than 160°C which corresponds to quality requirements imposed by the quality standard ASTM D 6751. Due to the higher flash point of methyl esters, the resultant flash point of the biodiesel blends gradually increases with increase of FAME content.

RESULTS & DISCUSSIONS

The lubricity is defined by the ability to reduce friction and wear on surfaces under load and relative motion. Generally, smaller wear scar signifies greater lubricity that ensures the effectiveness of interfacial lubricant fuel film on the separating action of these surfaces. This thin film is formed by adsorption of polar molecules of fuel on metal surfaces. Lubricity increases somewhat with chain length. However, the lubricity-enhancing effects of double bonds are greater than that of extended chain length. The wear scar value of neat methyl linolenate and methyl linoleate is low incomparison to methyl oleate and methyl stearate. The methyl palmitate shows higher wear scar value in HFRR in comparison to above mentioned esters [11].

From the HFRR wear scar value of neat esters, the SOME shows low value in comparison to Dillo and Palm Oil

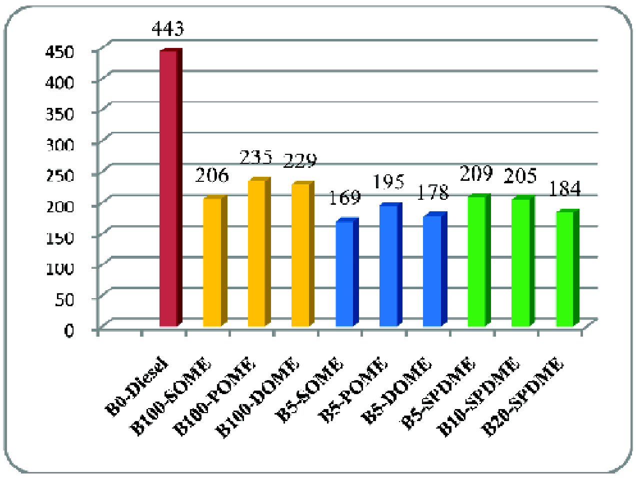

Fig-2: Wear scar, mm by HFRR

and hence better lubricity. DOME shows lower wear scar over POME due to presence of more methyl linoleate content. it shows that the mixture of the biodiesels derived from these three oils in equal ratios shows better lubricity value in HFRR data in comparison to the individual esters. The mixture of the different fatty acids of different oils contributes towards lower wear scar value as per HFRR test results.

CONCLUSIONS

In this study, the test results obtained with the high-frequency reciprocating rig (HFRR) lubricity tester give clear data concerning such factors as the influence of different fatty acid composition of vegetable oils on lubricity. The effects of blending compounds found in biodiesel on petrodiesel lubricity observed in the test results of mixture of fatty ester blend. This concluded that fatty compounds possess better lubricity than hydrocarbons, because of their polarity-imparting O atoms. Also, Lubricity improves somewhat with the chain length and the presence of double bonds.

ACKNOWLEDGEMENT

Author is gratefully acknowledging the management of IndianOil Corporation Ltd, Marketing Division for giving the permission to present this paper in NTC2016. We sincerely acknowledge to Sh R Mahapatra, IOC, R&D Scientist for carry out the required testing of biodiesel samples.

REFERENCES

[1] Industry Manual on Operation, Quality and safety for Biodiesel B100 & B5 – 2016.

[2] Gerhard Knothe et.al "Lubricity of Components of Biodiesel and Petrodiesel" – Energy & Fuels Vol.19, No-3, June 2005.

[3] Indian Standard IS 16531:2016 – Biodiesel, Diesel Fuel Blend (B6 to B20) Specification.

[4] Indian Standard IS-15607:2016 - Biodiesel (B100) Fatty Acid Methyl Esters (FAME) Specification.

[5] ASTM D6751- "Standard specification for Biodiesel Fuel Blend Stock (B100) for Middle Distillate Fuels".

[6] ASTM D6079 – "Standard test method for evaluating lubricity of diesel fuels by High – Frequency Reciprocating Rig (HFRR).

[7] Gerhard Knothe "Dependence of biodiesel fuel properties on the structure of fatty acid alkyl esters", Fuel processing technology – vol 86, issue-10 june 2005.

[8] Ramaraju A et.al. " Biodiesel Development from High Free Fatty Acid Punnakka Oil" : ARPN Journal of Engineering and applied Sciences, Vol-6, No-4,April 201.

[9] Rahul K Bawane et.al, " Performance test of CI engine fueled with Undi oil Biodiesel under variation blend proportion,compression ratio and engine load"- International journal of science, vol-3,issue-8,2014.

[10] F.Yasar et.al, " Comparing the lubricity of different biodiesel fuels," – 6th International advanced Technologies symposium,Turkey.

[11] Joseph PV et.al, "Study of some non-edible vegetable oils of Indian origin for lubricant application"- Journal of Synthic Lubrication, vol-34,Aug2007.

FZG gear test rig

The FZG gear test rig is a test machine with a mechanical power circuit. The drive gearbox and the text gearbox are frictionally engaged by two torque shafts (hereinafter only mentioned as shafts). For load application a clutch is provided on shaft 1. The temperature in the test gearbox can be set and controlled. The test rig is driven by an electric motor. The speed is 1,500 rpm. The variable-speed test rig allows speeds from 100 rpm to 3,000 rpm and two directions of rotation. The load can either be applied by a weight system or a the tension ratchet or with a automatically load system.

Highlights

- Delivered worldwide to more than 200 reputable customers
- Standards: ISO 14635, CEC-L-07, IP 334, ASTM D 5182, ASTM D 4998, FVA 243, FVA 54, FVA 2
- Option: Wear at low speed
- 2 oil units possible
- Siemens control with colour LCS
- Curve display
- Determination of scoring load capacity of oils
- Pitting test to determination the effects of various transmission oils and additives on gears
- Micropittings test to determine the effects of additives and oils on the occurrence of micropittings
- Shear stability test to determine the frictional losses of multi-grade oils

Technical data

- Speed : 100   3,000 rpm
- Two directions of rotation
- Max. torque: 715Nm (pinion)
- Max. oil temperature: 120°C (dip)/90°C (inject)
- Center distance: 91,5mm

Also Available

- Transmission Axle efficiency Test Rig
- Back to Back Planetary Gear Test Rig
- Bearing Test Rig for Turbocharger
- Turbine Wheel / Compressor Wheel Test Rig
- Gear Test Rig for Noise Test
- Clutch Test Rig
- Drive Shaft Test Rig
- Anti-Friction Bearing Test Rig
- Axle Bearing Fatigue Test Rig
- Worm Gear Test Rig
- Bevel Gear Test Rig
- Hypoid Ger Test Rig
- Four Square Gear Test Rig for Fatigue & Strength Testing
- Variable Centre Distance Gear Test Rig
- Endurance Test Rig

STRAMAMPS

Strama-MPS Maschinenbau GmbH & Co. KG
Ittlinger Str. 195 . 94315 Straubing
Product manager FZG Christoph Wolf
christoph.wolf@strama-mps.de
Tel. +49 9421/739-164 . Fax +49 9421/739-200
www.strama-mps.de

For Details Contact :
Tribotech Technologies Pvt. Ltd.
Mobile : +91 9810077557
+91 9810377557
E-mail : ttpl.ttpl@gmail.com


DUCOM
Material Characterization Systems
THE MOST ACCURATE AND REPEATABLE
FOUR BALL TESTER
IN THE MARKET
TRUSTED BY OVER 800 LABS WORLDWIDE
New updates in 2015!
Patented design (approval pending) for the "best-in-class" Extreme Pressure (EP), Wear Preventive (WP) & Friction measurement capabilities
TRIBOLOGY INSTRUMENTS
CONTRACT TESTING LAB
www.ducom.com | info@ducom.com
Ducom Instruments (America) • Ducom Instruments (Asia) • Ducom Instruments (Europe)